CM² MAGAZINE

第 101 期

南方科技大学海洋磁学中心主编

http://cm2.sustech.edu.cn/

创刊词

海洋是生命的摇篮，是文明的纽带。地球上最早的生命诞生于海洋，海洋里的生命最终进化成了人类，人类的文化融合又通过海洋得以实现。人因海而兴。

人类对海洋的探索从未停止。从远古时代美丽的神话传说，到麦哲伦的全球航行，再到现代对大洋的科学钻探计划，海洋逐渐从人类敬畏崇拜幻想的精神寄托演变成可以开发利用与科学研究的客观存在。其中，上个世纪与太空探索同步发展的大洋科学钻探计划将人类对海洋的认知推向了崭新的纬度：深海（deep sea）与深时（deep time）。大洋钻探计划让人类知道，奔流不息的大海之下，埋藏的却是亿万年的地球历史。它们记录了地球板块的运动，从而使板块构造学说得到证实；它们记录了地球环境的演变，从而让古海洋学方兴未艾。

在探索海洋的悠久历史中，从大航海时代的导航，到大洋钻探计划中不可或缺的磁性地层学，磁学发挥了不可替代的作用。这不是偶然，因为从微观到宏观，磁性是最基本的物理属性之一，可以说，万物皆有磁性。基于课题组的学科背景和对海洋的理解，我们对海洋的探索以磁学为主要手段，海洋磁学中心因此而生。

海洋磁学中心，简称 CM^2，一为其全名“Centre for Marine Magnetism”的缩写，另者恰与爱因斯坦著名的质能方程 $E = MC^2$ 对称，借以表达我们对科学巨匠的敬仰和对科学的不懈追求。

然而科学从来不是单打独斗的产物。我们以磁学为研究海洋的主攻利器，但绝不仅限于磁学。凡与磁学相关的领域均是我们关注的重点。为了跟踪反映国内外地球科学特别是与磁学有关的地球科学领域的最新研究进展，海洋磁学中心特地主办 CM^2 Magazine，以期与各位地球科学工作者相互交流学习、合作共进！

“海洋孕育了生命，联通了世界，促进了发展”。21 世纪是海洋科学的时代，由陆向海，让我们携手迈进中国海洋科学的黄金时代。

目录

1. 始新世-渐新世转型期间半球温度不对称驱动的墨西哥湾降水增加

翻译人：盖聪聪 gaicc@sustech.edu.cn

Hou M, Zhuang G, Ellwood B B, Liu X, et al. ***Enhanced precipitation in the Gulf of Mexico during the Eocene–Oligocene transition driven by interhemispherical temperature asymmetry*** [J]. Geological Society of America Bulletin, 2022.

http://doi.org/10.1130/B36103.1

摘要：研究表明，在始新世—渐新世过渡期（EOT），北半球海面温度（SST）下降幅度小于南半球。这种半球间的温度不对称与大西洋经向翻转环流（AMOC）的加强有关。AMOC 的加强可能推动了低纬度地区降水和风化的增加，以及随后大气二氧化碳的减少。然而，低纬区并没有定量的古降水记录，以至于无法评估 EOT 期间 AMOC 的影响。本文展示了来自墨西哥湾的高分辨率（每个样品约 6 k.y.）同位素和生物标志物记录。叶蜡碳同位素重建的降水记录在 EOT（34.1-33.6 Ma）期间增加了 44%，伴随着始新世最晚期 SST 约 2℃的长期增加。作者将墨西哥湾降水的增加归因于热带辐合带的向北移动，这是由南半球极地-热带温度梯度加大和 AMOC 的活跃所推动的。这一发现将经向温度梯度和大规模海洋环流的变化与低纬陆地水文气候联系起来，并提供了古水文证据，支持 EOT“温室”到“冰室”转换期间 CO_2 的风化反馈观点。

ABSTRACT: Studies reveal that the sea-surface temperature (SST) of the Northern Hemisphere decreased at a smaller amplitude than that of the Southern Hemisphere during the Eocene–Oligocene transition (EOT). This interhemispheric temperature asymmetry has been associated with intensified Atlantic Meridional Overturning Circulation (AMOC) that may have driven enhanced precipitation and weathering in low latitudes and the subsequent drawdown of atmospheric carbon dioxide. However, no quantitative constraints on paleo-precipitation have been reported in low latitudes to characterize the AMOC effect across the EOT. Here, we present the results of high-resolution (ca. 6 k.y. per sample) isotopic and biomarker records from the Gulf of Mexico. Reconstructed precipitation using leaf wax carbon isotopes shows an increase of 44% across the EOT (34.1–33.6 Ma), which is accompanied by a

secular increase in SST of ~2 ℃ during the latest Eocene. We attribute the enhanced precipitation in the Gulf of Mexico to the northward shift of the Intertropical Convergence Zone that was driven by an enlarged polar-tropic temperature gradient in the Southern Hemisphere and an invigorated AMOC. Our findings link changes in meridional temperature gradient and large-scale oceanic circulation to the low-latitude terrestrial hydroclimate and provide paleohydrological evidence that supports CO2-weathering feedback during the EOT "greenhouse" to "icehouse" transition.

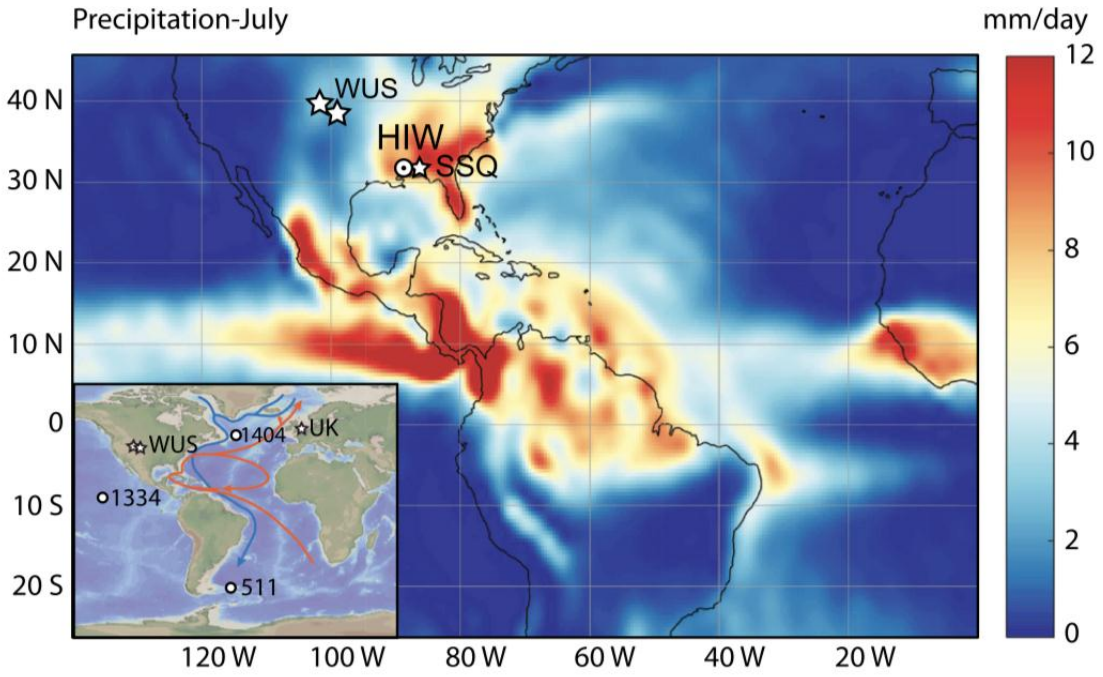

Figure 1. Modern boreal summer precipitation is plotted. The maximum precipitation in the tropics marks the northernmost position of the Atlantic Intertropical Convergence Zone in boreal summer. The Hiwannee (HIW) core site is marked with a circle. Precipitation data (mm/day) are derived from the National Centers for Environmental Prediction/National Center for Atmospheric Research reanalysis data set for the period 1981–2010. Inset shows the locations of sea-surface temperature records (circles) from Integrated Ocean Drilling Program Sites 511 and 1404 (Liu et al., 2009, 2018) and terrestrial paleoclimate records (stars) from the western United States (WUS) (Zanazzi et al., 2007; Fan et al., 2017), St. Stephens Quarry (SSQ) (Katz et al., 2008; Miller et al., 2008; Wade et al., 2012; Houben et al., 2019), and the UK discussed in the text (Hren et al., 2013); blue (deep currents) and orange (surface currents) curves are sketches of Atlantic Meridional Overturning Circulation (AMOC).

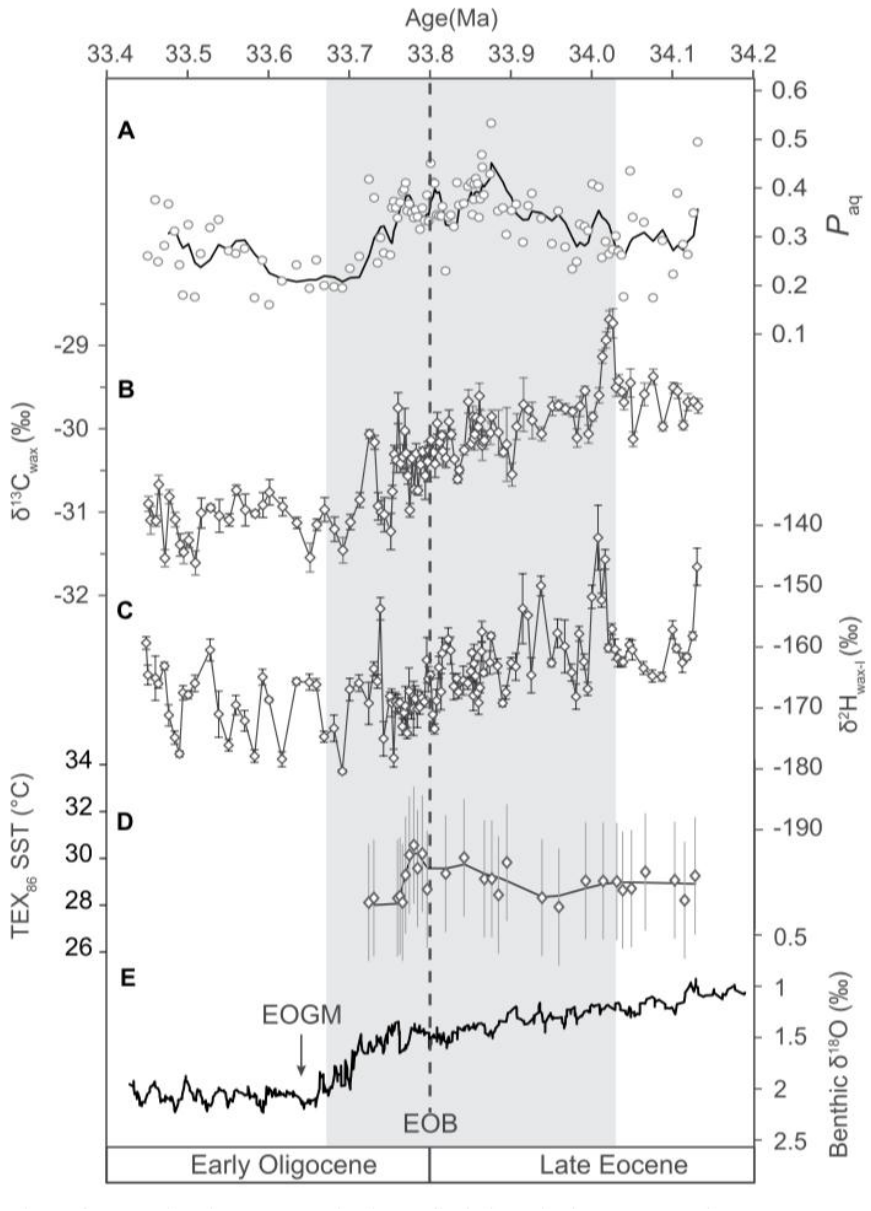

Figure 2. Paleoclimatic reconstruction in the Gulf of Mexico is based on leaf wax carbon and hydrogen isotopes and TEX_{86} sea-surface temperatures (SSTs). (A) P_{aq} record; black curve is generated by Loess regression. (B) $\delta^{13}C_{wax}$ record. (C) $\delta^{2}H_{wax-I}$ record. (D) TEX_{86} SSTs, with branched and isoprenoid tetraethers (BIT) < 0.5 and a calibration error of ±2.5 ℃; black curve is generated by local regression. SSTs with BIT > 0.5 are reported in the Supplementary Material (see footnote 1). (E) A global compilation of benthic $\delta^{18}O$ records with the black line represents a 10-point moving average (Cramer et al., 2009). The shaded bar denotes the Eocene–Oligocene transition (EOT) interval. EOGM—early Oligocene glacial maximum; EOB—Eocene–Oligocene boundary.

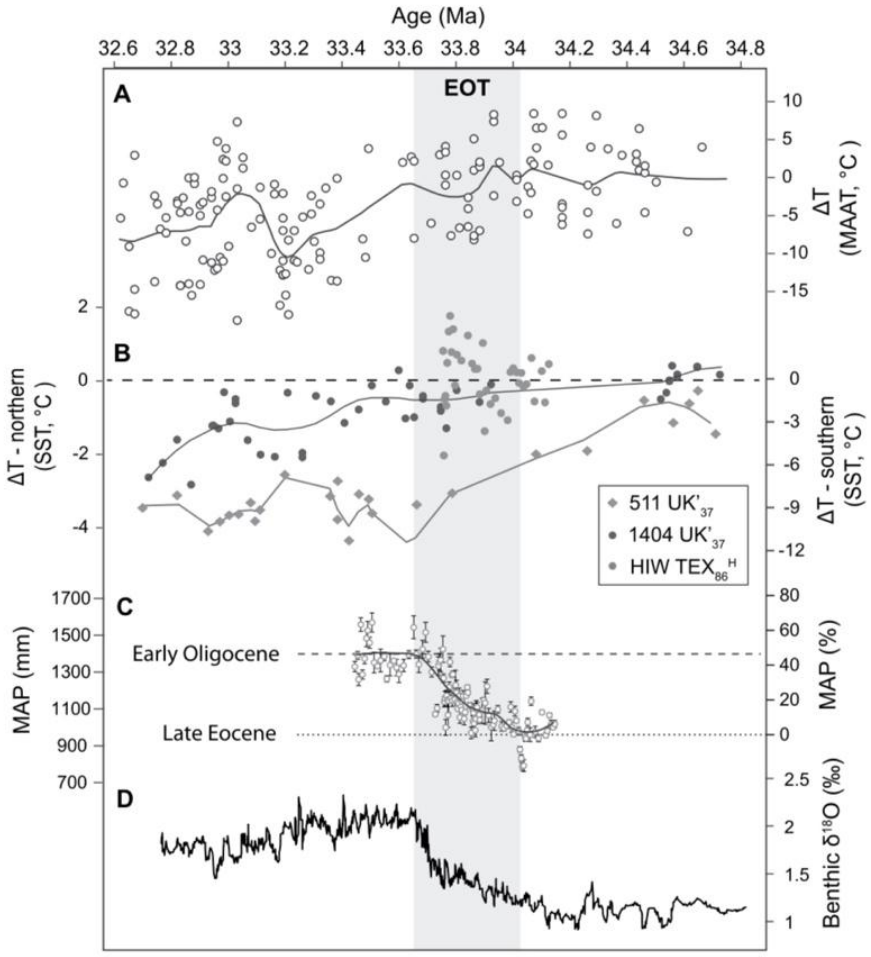

Figure 3. Comparison of leaf wax isotope-based rainfall variations and temperature records in both hemispheres is shown. (A) Change in mean annual average temperature (MAAT) from continental records (Zanazzi et al., 2007; Hren et al., 2013; Fan et al., 2017); data are smoothed by local regression (curves). (B) Sea-surface temperatures (SST) from sites 511 (North Atlantic) and 1404 (South Atlantic) (Plancq et al., 2014; Liu et al., 2018) and new TEX_{86} at Hiwannee (Gulf of Mexico). Temperature changes (ΔT) are relative to the mean values between 34.5 Ma and 37 Ma at individual localities. SSTs in sites 511 and 1404 (points) are smoothed by local regression (curves). (C) Reconstructed mean annual precipitation (MAP) based on $\delta^{13}C_{wax}$; dashed line represents the average MAP for the early Oligocene (33.45–33.70 Ma); dotted line denotes the average MAP for the late Eocene (before 34.0 Ma). Change of MAP in percentage (MAP%) is calculated relative to the mean values for the late Eocene (before 34.0 Ma) and is reported in percent (%). The shaded bar denotes the Eocene–Oligocene transition (EOT) interval. (D) Global benthic $\delta^{18}O$ records with a 10-point moving average (Cramer et al., 2009).

2. 磁小体铁同位素意义以及中中新世适宜期海洋地球化学变化

翻译人：蒋晓东 jiangxd@sustech.edu.cn

Havas R, Savian J F, Busigny V. ***Iron isotope signature of magnetofossils and oceanic biogeochemical changes through the Middle Eocene Climatic Optimum****[J]. Geochimica et Cosmochimica Acta. (2021) 311 332-352.*

https://doi.org/10.1016/j.gca.2021.07.007

摘要：趋磁菌能够在细胞内矿化形成磁铁矿晶体并在地质历史中保存下来。当趋磁菌死后磁小体化石就具有重要的古环境重建价值，这些磁小体很可能代表了地球最早的生物矿化。假定的源于生物的磁小体化石发现于古老陆地还是天体样品仍然还具有争议，此外它的古气候意义仍然还不清楚。我们对取自印度洋 ODP 711 孔的中中新世气候适宜期（MECO）的沉积物样品进行研究，该时段沉积物存储了大量的磁小体化石。我们第一次讨论了磁小体化石铁同位素作为生物标志物的潜在意义，并基于主微量元素地球化学分析描述了 MECO 相关的古环境事件。全岩铁同位素呈现出有限的变化-0.13±0.04‰ (n = 24)，这一信号与碎屑铁相关而不是趋磁菌的活动。因此我们应用化学方法提取特定的磁铁矿组分，并讨论了该方法的分析偏差并对数据进行校正。在磁小体富集的区段之外，氧化物的铁同位素组成呈现出较小的变化范围，平均值为-0.54±0.05‰。该特点很可能反映了热液的贡献，显著的 Eu 正异常也支持这一结果。相反，磁小体富集区段氧化物的铁同位素显示出较大的变化，从-0.12 到-0.94‰，在层位中呈现向上降低的趋势。这一层位很可能记录了大气气溶胶增强的铁输入，增强了生物生产力，随后在孔隙水中形成含铁的条件。铁同位素和 Mn/Fe 的同步变化很可能归因于与成岩作用密切相关的氧化还原梯度的垂向变化。沉积物中有机质降解重晶石沉淀，很可能通过降低孔隙水 SO_4^{2-}的浓度而促进磁小体化石测保存，以及随后的 H_2S 的形成。最后我们对孔隙水通量的演化建立了模型，估算了磁小体和流体之间铁同位素的分馏△$^{56}Fe_{mag\text{-}Fe(II)aq}$ = 0.1 – 0.3‰，这一值显著区别于非生物磁铁矿的分馏(~1.5‰)。与近期室内培养趋磁菌相反，本研究中观察到非质量分馏的铁同位素。虽然这样，但本研究中多样的地球化学指标提供了重要的古气候和磁小体生物演化的约束。

ABSTRACT: Magnetotactic bacteria (MTB) intracellularly precipitate magnetite (Fe_3O_4) crystals that can be preserved in the geological record. When MTB die, the so-called magnetofossils constitute valuable proxies for paleoenvironmental reconstructions and are suspected to represent some of the oldest traces of biomineralization on Earth. Yet, the biogenicity of putative magnetofossils found in ancient terrestrial and extra-terrestrial samples is still largely debated and their significance for past climate still holds uncertainties. Here we studied a sedimentary sequence from the Indian Ocean (ODP Hole 711A) recording the Middle Eocene Climatic Optimum (MECO) through which a magnetofossil-rich interval was deposited. We investigated for the first time the potential of Fe isotopes as a biosignature in magnetofossils and thoroughly describe MECO related paleoenvironmental disruptions based on major and trace element concentrations. Bulk sediment Fe isotopes showed limited variations, with δ^{56}Fe around -0.13 ± 0.04‰ (n = 24), linked to detrital iron rather than MTB activity. Hence, a sequential chemical extraction protocol was applied to determine the specific composition of magnetite. We discuss analytical biases related to this protocol (i.e. partial phyllosilicate and Mn-oxide leaching) and apply corrections to the data. Outside the magnetofossil-rich interval, Fe isotope compositions of oxides (mainly biotic and/or abiotic magnetites and possibly Fe coprecipitated with Mn-oxides) display a small range averaging -0.54 ± 0.05‰, and are interpreted as reflecting dominantly hydrothermal contribution, a conclusion also supported by prominent Eu anomaly. In contrast, the magnetofossil-rich interval shows larger δ^{56}Fe variability in oxides, from -0.12 to -0.94‰, decreasing upwards in the stratigraphic section. This interval likely records enhanced Fe supply from atmospheric fallout, increase in biological productivity (illustrated by increased Ba accumulation rate) and subsequent development of ferruginous conditions in the sediment porewater. Covariations of Fe isotope compositions and Mn/Fe ratios can be explained by a vertical migration of a redox front and associated diagenetic modifications. Precipitation of barite ($BaSO_4$) in the sediments after organic matter decay probably favored the preservation of magnetofossils by decreasing SO_4^{2-} concentration in porewaters and subsequent H_2S production, which usually dissolve magnetite in the sulfidic zone. Finally, we model the evolution of porewater fluid and estimate Fe isotope fractionation between magnetofossils and fluid to $\triangle^{56}Fe_{mag\text{-}Fe(II)aq}$ = 0.1 – 0.3‰, a value significantly different from abiotic magnetite fractionation (~1.5‰). Contrasting with recent results on MTB laboratory culture,

no mass independent fractionation of Fe isotopes was observed in the present study. Nevertheless, the diverse geochemical proxies presented here provide important constraints on paleoclimate and magnetofossil biogenicity evaluation.

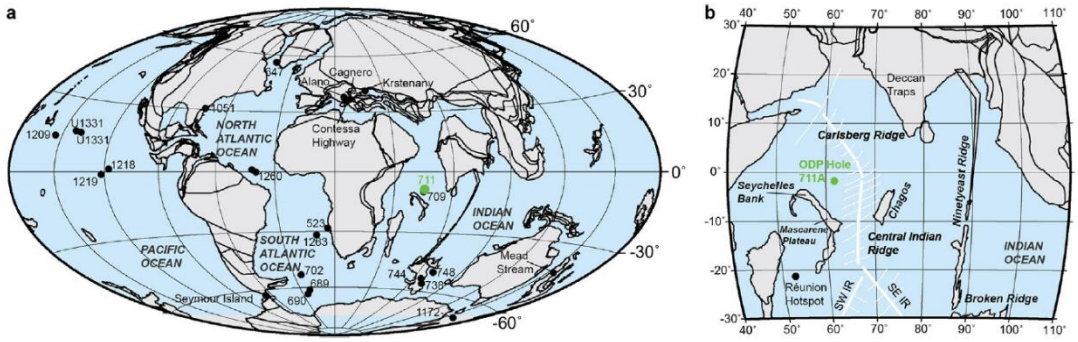

Figure 1. Map showing paleo-position on a 40Ma reconstruction (a) and present position (b) of ODP Site 711A (green dot) and other sites were the MECO event has been reported (black dots on left figure) (modified from Savian et al., 2016). The maps were plotted using a paleogeographic reconstruction created using the Ocean Drilling Stratigraphic Network (GEOMAR, Kiel, Germany) website. Considering a half spreading rate of about 1.5 cm/yr since ~45 Ma (Merkouriev and Sotchevanova, 2003), ODP Site 711A would have lied less than 100 km away from the central Indian and Carlsberg ridges at the time of the MECO event (schematically represented in white here; SW IR and SE IR on right figure stand for South West and South East Indian Ridges, respectively). (For interpretation of the references to colour in this figure legend, the reader is referred to the web version of this article.)

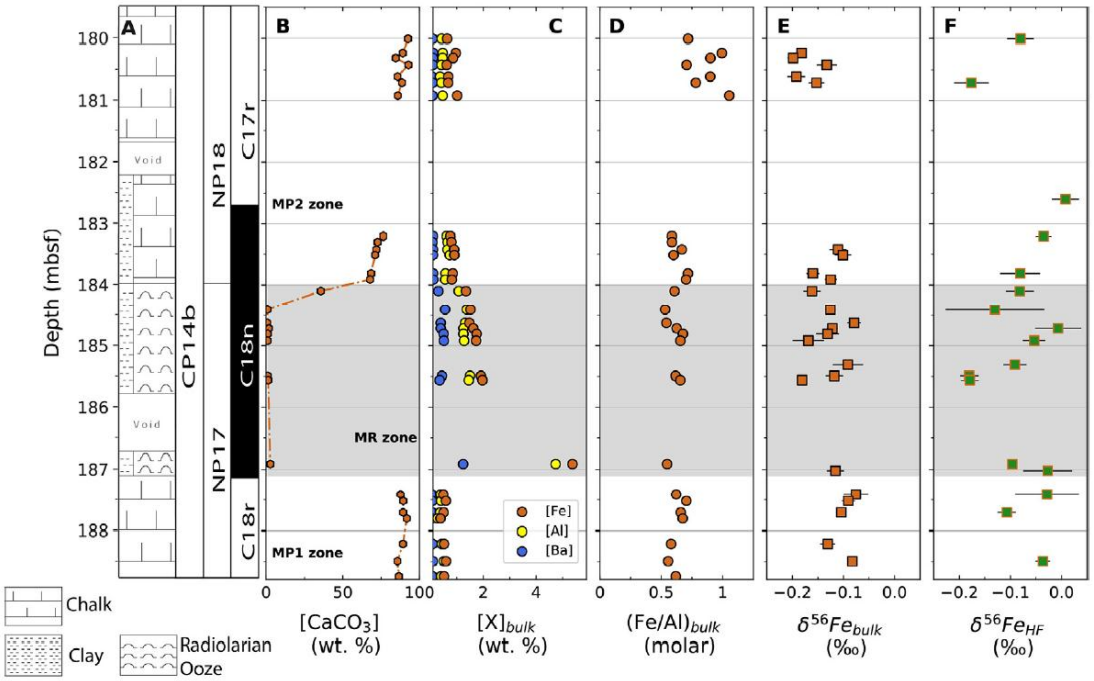

Figure 2. Stratigraphic variations of selected geochemical indicators in the bulk sediment and HF fraction (see subscript bulk or HF on axis title). (A) From left to right: lithological log (modified after Backman et al., 1988), calcareous nannofossil zonation (Okada and Bukry, 1980; Martini, 1971) and magnetic polarity sequence (modified after Savian et al., 2016). (B) Calcite concentrations, which approach 0 in MR zone, indicating that Hole 711A lied below the CCD at this time. (C) Fe and Al concentrations. (D) Fe/Al molar ratios. Iron isotope compositions in (E) bulk sediment and (F) HF fraction. Both d56Fe values exhibit similar and restricted values and no clear stratigraphic trend. Error bars correspond to 1r values. Following Savian et al. (2013), the MECO's peak (~40 Ma) would occur at the start of MR zone.

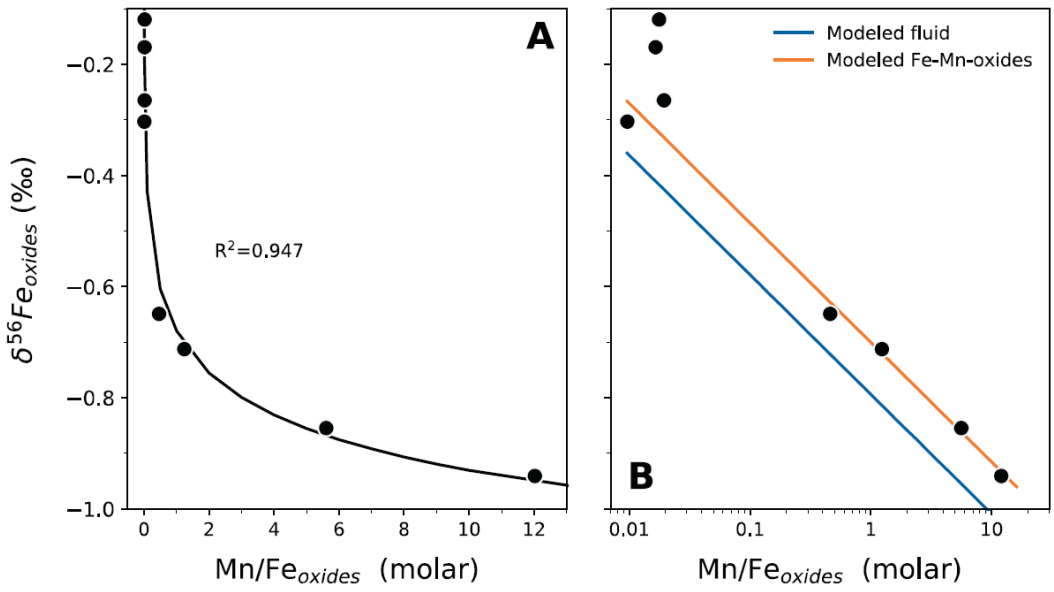

Figure 3. Evolution of δ^{56}Fe versus Mn/Fe molar ratio in MR zone samples for the ‘‘oxide fraction” (i.e. silicate-corrected oxalate fraction). (A) Solid black line represents the logarithmic linear regression curve fitting the data (y = _1.109ln(x)_0.6798, correlation coefficient R2 = 0.947). (B) Comparison between the fluid (blue) and Fe-Mn oxides (orange) isotopic composition modeled with Rayleigh fractionation equations and the ‘‘oxide fraction” data. The modeled δ^{56}Fe of Fe-Mn oxides (orange) represents Fe included in magnetites and possibly Mn-oxides forming in diverse redox conditions (see main text for details). The calculated initial fluid composition and fractionation factor are 0.36‰ and 0.09‰, respectively. The four Mn-depleted samples (187.02, 186.91, 185.46 and 185.49 mbsf) have similar Mn/Fe lying close to 0 but variable d56Fe and thus cannot be perfectly fitted. Relative to the modeled fluid, at similar Mn/Fe ratios, they express a fractionation ranging from ~0.06 to 0.30‰. (For interpretation of the references to colour in this figure legend, the reader is referred to the web version of this article.)

3. 磁铁矿退磁能与内部应力-随温度变化的磁滞测量

翻译人：张琪 zhangq7@sustech.edu.cn

Béguin A, Fabian K, ***Demagnetization Energy and Internal Stress in Magnetite From Temperature-Dependent Hysteresis Measurements*** *[J]. Geophysical Research Letters, 2021, 48, 24.*

https://doi.org/10.1029/2021GL096147

摘要：磁铁矿的磁化状态控制着地球和行星岩石中剩磁的获取与稳定性。虽然通常认为粒径大小很重要，但应力、颗粒形状和静磁相互作用也可以从本质上改变其磁稳定性。本文中，作者发现，当各向异性是由退磁能引起时，磁滞回线接近饱和(ATS)中的比例可逆(SRW)与温度无关。应力各向异性随温度升高而消失。新的测量和评价方法，将应力诱导的各向异性与退磁效应分离开来。作者使用不同应力和退磁条件下的理论 ATS 曲线对新方法进行了校正。合成磁铁矿样品的实验结果支持了此方法的有效性，并为静磁、磁晶和应力能之间的关系提供了见解。SRW 方法为研究古地磁记录机制的可靠性提供了一种新的工具，可以定量研究构造、陨石撞击、氧化、溶解或淬火引起的应力。

ABSTRACT: The magnetization state of magnetite controls acquisition and stability of remanent magnetization in Earth and planetary rocks. Although commonly interpreted in terms of grain size, also stress, grain shape, and magnetostatic interactions can substantially modify magnetic stability. Here, we show that scaled reversible work (SRW) in the approach-to-saturation (ATS) of hysteresis curves is temperature independent if anisotropy is due to demagnetizing energy. Stress anisotropy vanishes with increasing temperature. With a new measurement and evaluation procedure stress-induced anisotropy is separated from demagnetization effects. We calibrated the new method using theoretical ATS curves for different stress and demagnetization regimes. Experimental results for synthetic magnetite samples underpin the validity of the method and provide insight into the relationship between magnetostatic, magnetocrystalline, and stress energies. The SRW method provides a new tool to study the reliability of paleomagnetic recording mechanisms, and enables quantitative investigation of stresses due to tectonics, meteorite impacts, oxidation, exsolution, or

quenching.

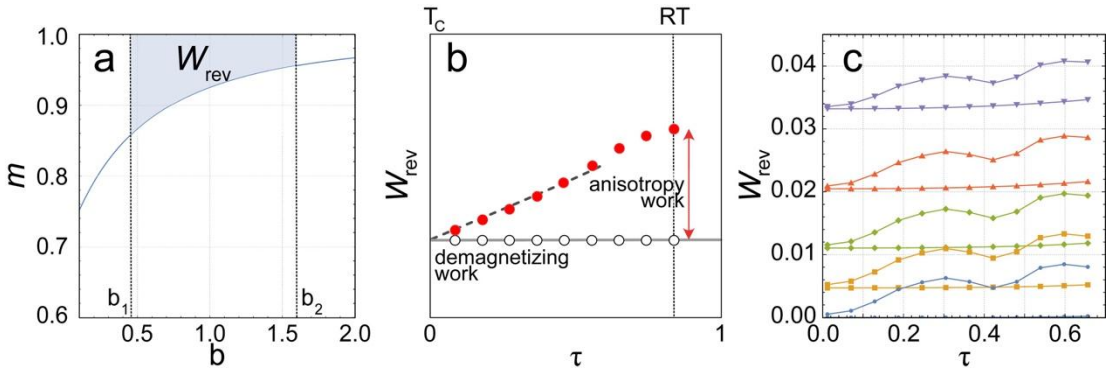

Figure 1. (a) Scaled plot of the reversible approach-to-saturation (ATS) part of a hysteresis curve (blue line). Scaling of the magnetization to $m = M/M_s$ and of the field to $b = B/J_s$ leads to unit free quantities. The shaded area represents w_{rev} in the scaled field interval $[b_1, b_2] = [0.45, 1.6]$, in this sketch $w_{rev} = 0.092$. (b) Theoretical behavior of w_{rev} as a function of scaled temperature τ. If scaled reversible work (SRW) is exclusively due to demagnetizing energy, w_{rev} is independent of temperature (circles). Other anisotropies decay with increasing temperature (red dots), so only demagnetizing work remains when extrapolating to $\tau = 0$ (dashed line). (c) Calculated SRW from ATS models for magnetite with varying $\Delta N = 0$, 0.1, 0.2, 0.3, and 0.4 (blue, orange, green, red, and purple). Horizontal curves are for stress-free models and sloped curves are for $\sigma = 300$ MPa, where the model calculations use magnetostriction constants $\lambda_{111}(T)$ from experimental data, which lead to the maxima and minima at $\tau = 0.3$, 0.42, and 0.6.

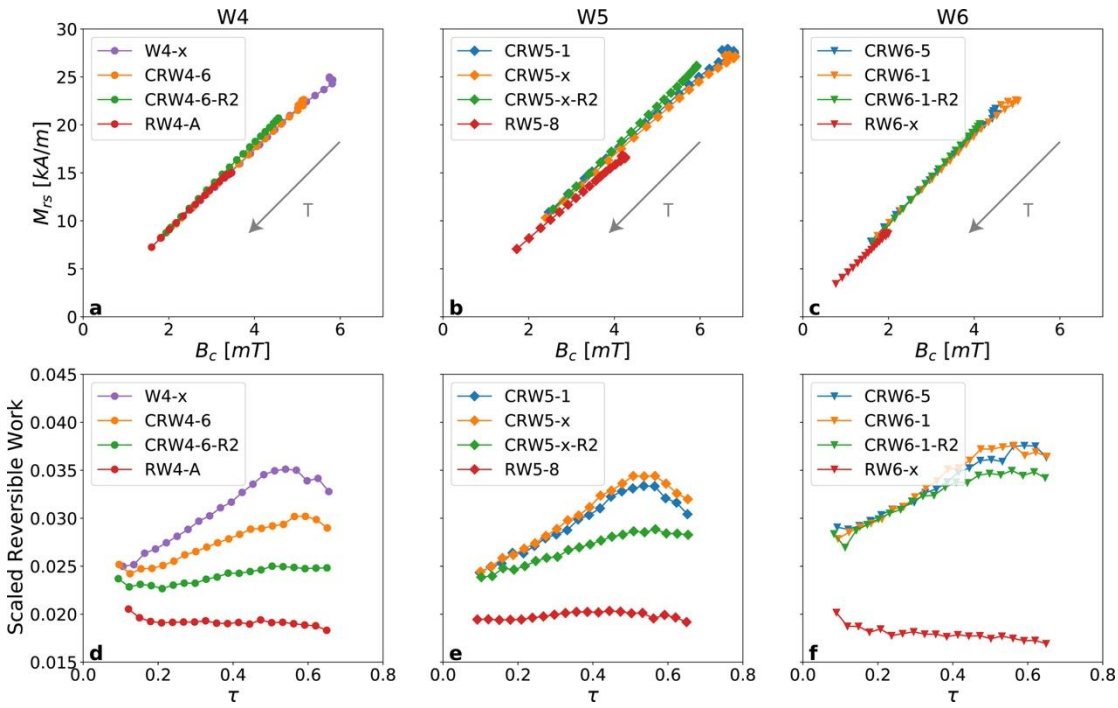

Figure 2. Plots of $M_{rs}(T)$ versus $B_c(T)$ measured between 25 ℃ and 500 ℃ for W4 (a), W5 (b), and W6 (c). Specimen names include treatment options: R, reduced; CR, crushed reduced. Both M_{rs} and B_c decrease with increasing temperature. Higher values are obtained for stressed (crushed: blue and orange; oxidized: purple) specimens compared to uncrushed specimens (red). Repeated annealed runs (green) have similar linear tends with temperature slightly lower values for M_{rs} and B_c. The scaled reversible work w_{rev} versus normalized temperature τ is plotted for W4 (d), W5 (e), and W6 (f). For all reduced uncrushed specimens (red) w_{rev} is essentially constant. Crushed specimens (orange or blue) have larger w_{rev} also in the limit $\tau \rightarrow 0$. This is true also for oxidized specimen W4 (d: purple). Annealed repeat runs (green) have reduced w_{rev} but the same limit $\tau \rightarrow 0$ as unannealed counterparts (orange and blue).

4. 后期沉积成岩改变对铁和钼相关氧化还原指标的影响

翻译人：仲义 zhongy@sustech.edu.cn

Suemeyya Eroglu, FlorianScholz, Renato Salvatteci., et al., ***The impact of postdepositional alteration on iron- and molybdenum-based redox proxies*** *[J] Geology, 2021, 49(12), 1411-1415.*

https://doi.org/10.1130/G49291.1

摘要：沉积岩石中活动（不活动性）性铁种、自生性钼含量以及自生钼（Mo）同位素通过现代海洋背景下氧化和缺氧环境的矫正，并用来重建过去海洋氧化还原状态的指标。然而，同沉积和沉积后期改造可能导致氧化还原指标的改变，从而对古重建的可靠性提出了挑战。作者展示了来自加利福尼亚和秘鲁沿岸两个最低含氧带地区现代有机质含量丰富的沉积物结果。结果显示，钼在沉积后不久与有机碎屑硫酸盐还原过程中产生的硫化氢（H_2S）反应并被完全固定下来。因此，沉积物深处产生的 H_2S（例如，通过硫酸盐还原甲烷厌氧氧化产生的 H_2S）不会改变最初沉积的 Mo 浓度和 δ^{98}Mo 结果，这支持了 Mo 相关的氧化还原指标的可靠性。相反，铁的种属结果显示由于铁矿物持续暴露于 H_2S 反应，黄铁矿反应持续发生。重要的是，与铁结核氧化物和碳酸盐结合（高活性 Fe）和低活性铁（例如片状硅酸盐）在早期成岩中都发生了黄铁矿作用。这个过程产生的铁相关指标性特征会错误地指示含铁或者缺氧环境。

ABSTRACT: Ratios of (un)reactive iron species, authigenic molybdenum contents (Moauth), and molybdenum isotope compositions ($\delta^{98}Mo_{auth}$) in sedimentary rocks are geochemical proxies that are widely used to reconstruct past marine redox states, which have been calibrated in modern marine settings covering oxic to euxinic conditions. However, syn- and postdepositional processes can result in alterations and ambiguities of proxy-derived redox signals that can challenge the validity of paleoreconstructions. We present new data from modern organic-rich sediments of two oxygen minimum zone settings in the Gulf of California and the Peruvian margin. The results show that Mo is fully immobilized shortly after deposition by reaction with hydrogen sulfide (H_2S) produced during organoclastic sulfate reduction. Thus, any H_2S produced deeper in the sediment (e.g., by sulfate reduction coupled to anaerobic methane oxidation) leaves the initially deposited Mo concentrations and δ^{98}Mo signatures unaltered, which supports the robustness of Mo-based redox proxies. In contrast, the Fe speciation data reveal continued pyritization due to constant exposure of

Fe minerals to H_2S. Importantly, both Fe bound to oxides and carbonates (highly reactive Fe) and also poorly reactive Fe (e.g., sheet silicates) undergo pyritization during early diagenesis. This process generates Fe-based proxy signatures that falsely imply ferruginous or euxinic conditions.

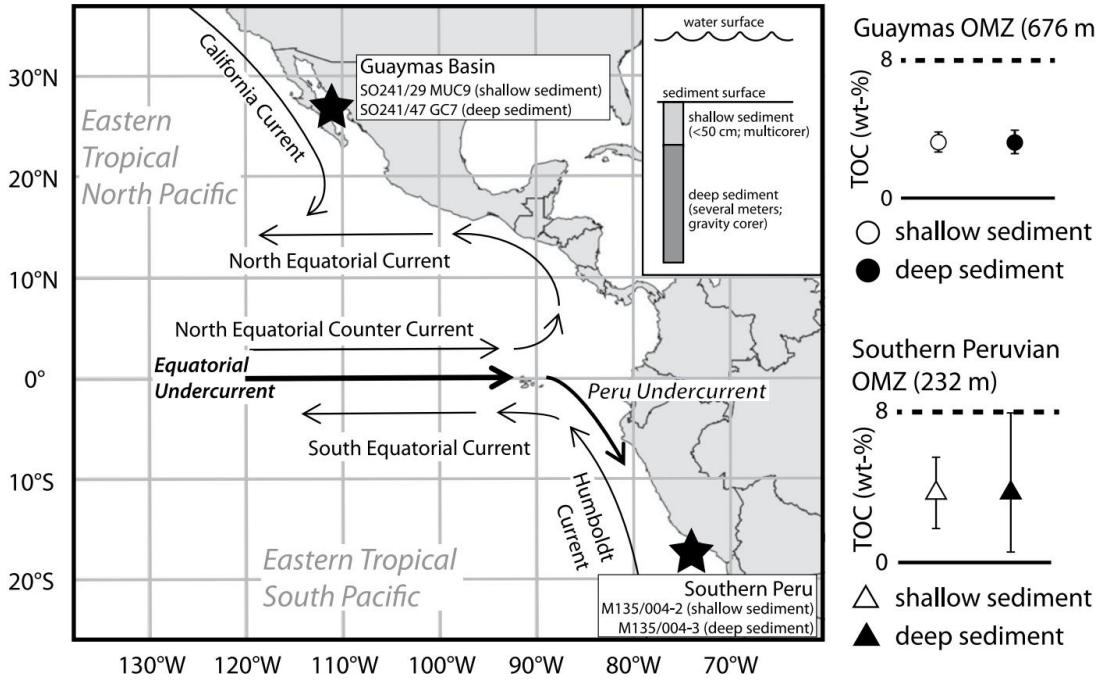

Figure 1. Overview of the major ocean currents in the eastern tropical North and South Pacific Oceans (ETNP and ETSP) (modified from the U.S. National Oceanic and Atmospheric Administration database, https://www. ncei.noaa.gov/products/ global-ocean-currentsdatabase/) and sampling locations. Sediments of the southern Peruvian oxygen minimum zone (OMZ) as well as the Guaymas OMZ (Gulf of California; Eroglu et al., 2020) are enriched in total organic carbon (TOC), as is shown by mean TOC values (±2SD) of shallow (<50 cm) and deep sediment (several meters).

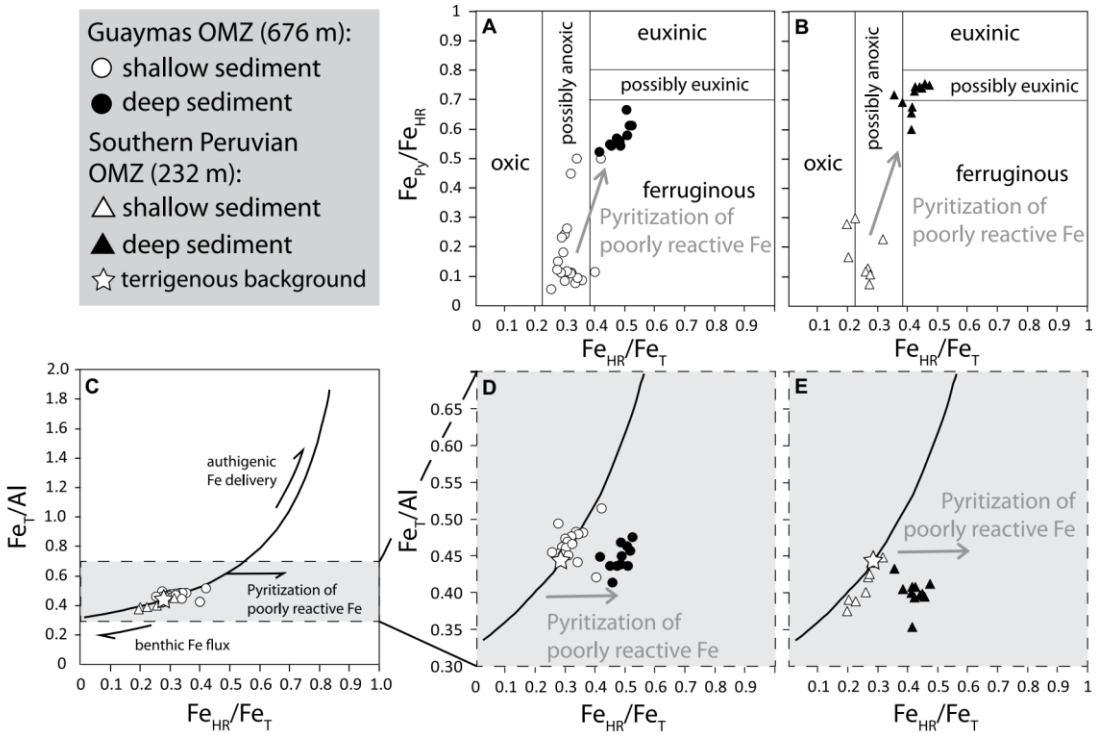

Figure 2. Fe speciation data from shallow and deep sediments (Fe_{HR}—highly reactive Fe; Fe_{Py}—pyrite; Fe_T—total Fe). (A,B) Cross-plot of Fe_{Py}/Fe_{HR} versus Fe_{HR}/Fe_T in Guaymas (Gulf of California) (A) and southern Peruvian (B) sediments showing fields that are indicative of oxic, anoxic-ferruginous, and anoxic-sulfidic conditions (Raiswell et al., 2001; Poulton and Canfield, 2011). (C) Cross-plot of Fe_T/Al versus Fe_{HR}/Fe_T of shallow sediments from the Guaymas and southern Peruvian oxygen minimum zone (OMZs). Trend line indicates net Fe enrichment/depletion of highly reactive Fe due to authigenic Fe delivery/sedimentary Fe release under anoxic conditions in the water column. Pyritization of poorly reactive silicate Fe results in increasing Fe_{HR}/Fe_T but constant Fe_T/Al. Open star represents terrigenous background sedimentation on the Peruvian margin (Scholz, 2018). (D) Fe_T/Al versus Fe_{HR}/Fe_T cross-plot of Guaymas shallow and deep sediments. (E) Fe_T/Al versus Fe_{HR}/Fe_T cross-plot of southern Peruvian shallow and deep sediments.

5. 印度夏季风对主要热带气候模式的正负相非对称响应

翻译人：杨会会 11849590@mail.sustech.edu.cn

Chakraborty A, Singhai P, ***Asymmetric response of the Indian summer monsoon to positive and negative phases of major tropical climate patterns [J].*** *Scientific Report, 2021, 11, 22561.*

https://doi.org/10.1038/s41598-021-01758-6

摘要：现有的与印度夏季风(ISM)有关的热带遥相关理论在方法上存在差异。因此，根据单一的物理机制，不同的热带气候模式对 ISM 的相对影响不能量化。本文中，我们表明与 ISM 有关的热带遥相关，可以通过由围绕印度的洋表压力（*Ps*）梯度驱动的净水分辐合来解释。主要热带气候模式的正负相位，调节这些在纬向和/或经向不对称的压力梯度，导致了水汽辐合和 ISM 降雨的不对称变化。厄尔尼诺时期的干旱比拉尼娜时期的洪水更强是因为，厄尔尼诺期间阿拉伯海向东传输的水汽流量降低幅度比在拉尼娜期间增加的幅度更大，这是由经向的 *Ps* 梯度比例变化导致的。当北半球夏季赤道大西洋 SST 和前一年冬季 ENSO 对印度夏季风降雨的影响显著，印度洋偶极子驱动的水汽辐合异常则影响不显著。此外，当由 Ps 的纬向和经向梯度的不对称变化导致的，ENSO 期间的印度夏季风降雨出现极值，那么，由纬向对称 Ps 异常的纬向梯度而产生的，非 ENSO 的印度夏季风降雨极值则变化增强。

ABSTRACT: The existing theories for the tropical teleconnections to Indian summer monsoon (ISM) are diverse in approaches. As a result, it is impossible to quantify the relative impacts of different tropical climate patterns on ISM, complying with a single physical mechanism. Here, we show that tropical teleconnections to ISM can be explained through net moisture convergence driven by surface pressure (*Ps*) gradients surrounding the Indian region. The positive and negative phases of major tropical climate patterns modulate these pressure gradients asymmetrically in the zonal and/or meridional directions leading to asymmetric changes in moisture convergence and ISM rainfall (ISMR). Stronger El Nino droughts than La Nina foods are due to greater decreased eastward moisture fux over the Arabian Sea during El Nino than the corresponding increase during La Nina driven by proportionate meridional *Ps* gradients. While the equatorial Atlantic Ocean's sea surface

temperature in boreal summer and El Nino Southern Oscillation in the preceding winter changes ISMR significantly, moisture convergence anomalies driven by the Indian Ocean Dipole were insignificant. Moreover, while ISMR extremes during ENSO are due to asymmetric changes in zonal and meridional gradients in Ps, non-ENSO ISMR extremes arise due to the zonal gradient in zonally symmetric *Ps* anomalies.

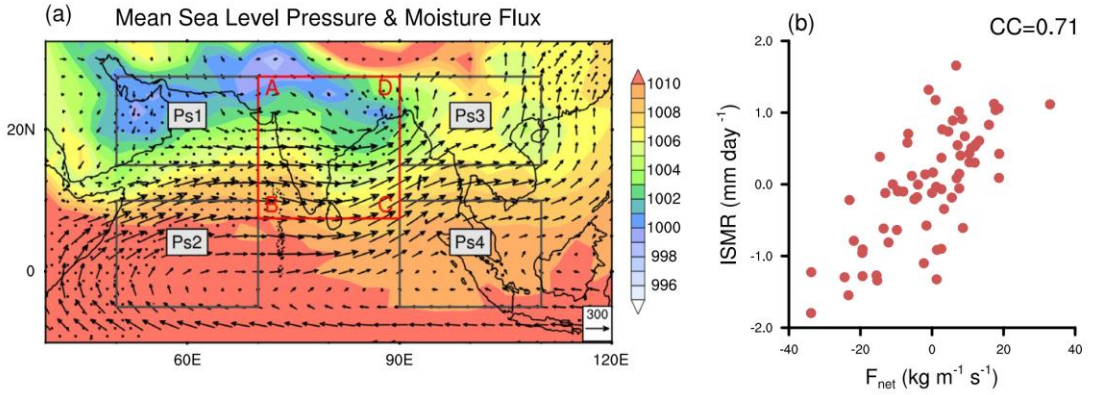

Figure 1. (a) Boreal summer season (June–September) climatological mean sea level pressure (MSLP) in hPa, along with vertically integrated moisture flux vectors ($kg\ m^{-1}s^{-1}$) during the 1948-2015 period. Te box ABCD represents the study region (7.5°–27.5°N, 70°–90°E). Te surrounding boxes represent the regions of surface pressure used for determining the incoming and outgoing moisture fluxes (*Ps1*: 15°–27.5°N, 50°–70°E, *Ps2*: 5°S–10°N, 50°–70°E, *Ps3*: 15°–27.5°N, 90°–110°E, *Ps4*: 5°S–10°N, 90°–110° E). (b) Te scatter of Indian summer monsoon rainfall (ISMR, only land points of region ABCD) versus net moisture convergence (F_{net}) over the entire region marked by ABCD. Inset value is for correlation coefficient (CC) between ISMR and F_{net} for 1948- 2015. Te dotted regions in Fig. 1a indicate a correlation coefficient between ISMR and F_{net}, which is significant at a 90% confidence level (using t-test). This figure was created using NCL version 6.4.0 (https://www.ncl.ucar. edu/).

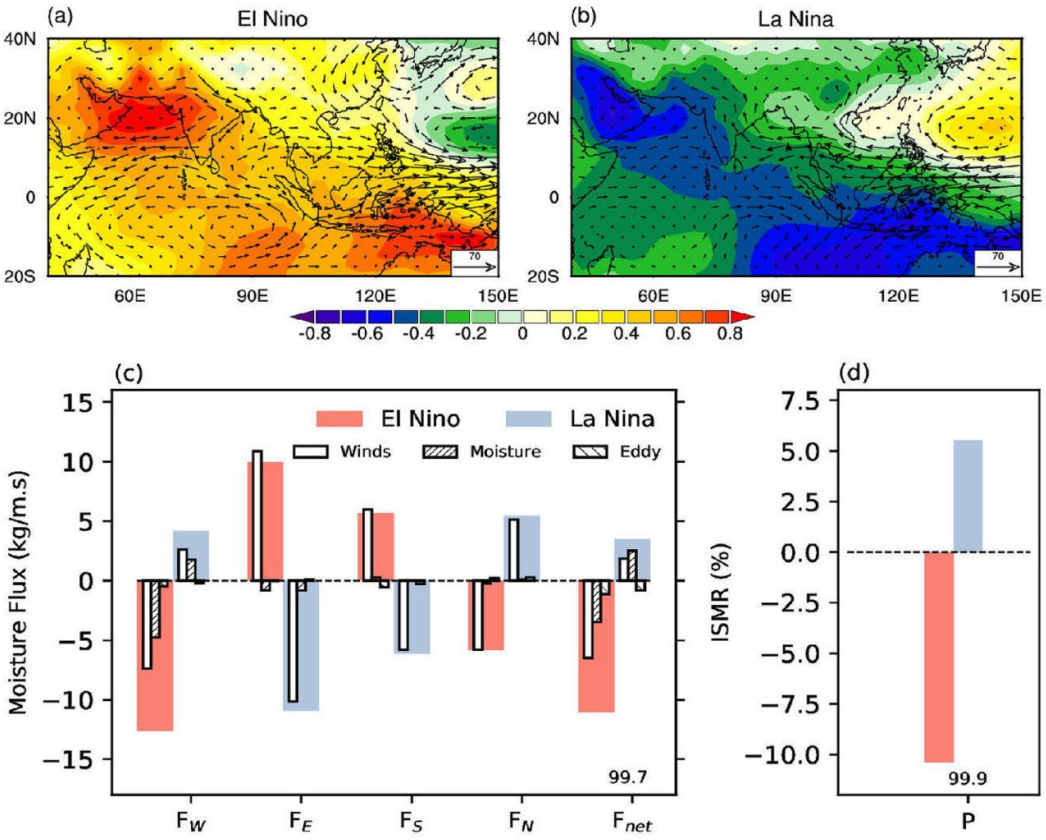

Figure 2. Te teleconnection to El Nino Southern Oscillation (ENSO). Composite change in the anomalous surface pressure hPa and vertically integrated moisture flux vector (kg $m^{-1}s^{-1}$) during (**a**) El Nino and (**b**) La Nina. (**c**) Shows the vertically integrated moisture flux anomalies and its decomposition along the four boundaries (west (F_W), east (F_E), south (F_S), and north (F_N)) and net moisture convergence (F_{net}) over region marked as ABCD in Fig. 1a, for El Nino (red) and La Nina (blue) years. Te contribution to total moisture flux (solid fill) and its components: due to winds (V q), moisture (V q), and eddy flux (V q). (**d**) Te corresponding change in the Indian summer monsoon rainfall (ISMR) during El Nino and La Nina. Te number along F_{net} and P represents the significance level at which the hypothesis that means are the same for ENSO years is rejected. This figure was created using NCL version 6.4.0 (https:// www. ncl. ucar. edu/).

6. 印度洋表面温度梯度逆转对印度洋夏季风的影响

翻译人：李海 12031330@mail.sustech.edu.cn

Weldeab S, Rühlemann C, Ding Q, et al. ***Impact of Indian Ocean surface temperature gradient reversals on the Indian Summer Monsoon*** *[J]. Earth and Planetary Science Letters, 2022, 578: 117327.*

https://doi.org/10.1016/j.epsl.2021.117327

摘要: 印度夏季风（ISM）降水是决定世界上人口最稠密地区生计的主要因素。ISM 的年际变率受多种气候变率模式的影响，包括印度洋东部、西部和东北部之间的异常季节性海面温度（SST）梯度逆转。随着全球变暖，预计印度洋纬向和经向海温梯度变化的频率将增加，但其对 ISM 的影响存在争议。在这里，作者提供了 2.5 万年的 SST 记录，并推断出恒河-雅鲁藏布江-梅赫纳河（GBM）径流，为 ISM 降水变化提供了一个空间综合测量。这一记录表明，当孟加拉湾地表水与赤道东印度洋之间的海温梯度反转时，ISM 系统呈现单调的去冰强化。我们假设经向海温梯度的逆转减小了海因里希事件 1 和新仙女木对 ISM 区低海拔部分的影响。此外，记录表明，全新世期间 ISM 的最大增强发生在 7900±470～5700±360，与印度洋纬向海温梯度的逆转和风场的变化相吻合，并存在因果关系，并由气候模拟结果推断和支持的。研究结果表明，印度洋的纬向和经向温度梯度的变化强烈影响了全新世季风加强的时间以及 ISM 对最后一次冰消期淡水强迫的响应。

ABSTRACT: Indian Summer Monsoon (ISM) precipitation is the main determinant of livelihood in a densely populated world region. The interannual variability of the ISM is influenced by several modes of climate variability, including anomalous seasonal sea surface temperature (SST) gradient reversals between the eastern, western, and northeastern Indian Ocean. With global warming, the frequency of zonal and meridional Indian Ocean's SST gradient changes is projected to increase but its impact on the ISM is debated. Here we present a 25,000-year proxy record of SST and inferred Ganges-Brahmaputra-Meghna (GBM) River runoff that provides a spatially integrated measure of ISM precipitation changes. This record indicates a monotonic deglacial strengthening of the ISM system when the SST gradient between the Bay of Bengal surface water and the eastern equatorial

Indian Ocean was reversed. We posit that the reversal in the meridional SST gradient reduced the impact of Heinrich Event 1 and Younger Dryas on the low elevation part of the ISM domain. Furthermore, the proxy record shows that the strongest Holocene ISM strengthening occurred between 7900±470 and 5700±360 years before present, coinciding with and causally linked to the reversal of the Indian Ocean zonal SST gradient and ensuing changes in the wind fields, a sequence of events that is inferred from and supported by the results of our climate simulation. Our study demonstrates that changes in the Indian Ocean's zonal and meridional thermal gradient strongly shaped the timing of Holocene monsoon strengthening and the response of ISM to the last deglacial freshwater forcing.

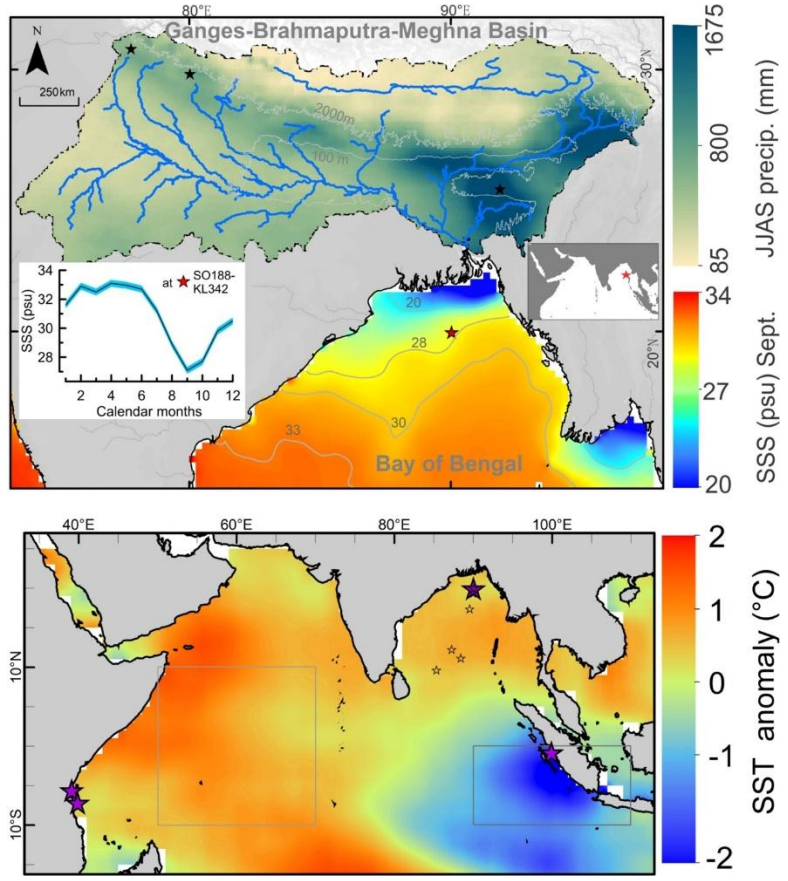

Figure 1. Setting of the study area (northern Bay of Bengal) within the broader Indian Ocean and bordering land masses. Upper panel: Color shading of the GBM Basin, indicating total precipitation from June to September (five-year average) (Huffman, 2017). Blue and gray lines indicate tributaries of GBM rivers and selected topographic elevation, respectively. Color shading and contours in the Bay of Bengal shows sea surface salinity (SSS) in September (4-year average) (Fore et al., 2016). Inset (left) depicts monthly SSS changes (Fore et al., 2016) (blue envelope: 2 sigma uncertainty) above SO188-342KL site which is indicated by a red star in the main figure. The black

stars in the GBM Basin indicate cave locations of stalagmites discussed below. Lower panel: pIOD conditions in 1997. SST anomaly of November 1997 relative to a 16-year average SST of November (Behringer and Xue, 2004)). Sites of cores whose data are used to reconstruct SST gradients are indicated by purple stars. Rectangles show areas whose SON SST is used to define the pIOD (Saji et al., 1999) and to create the modeled pIOD occurrence. Within the Bay of Bengal, the large and small symbols indicate the location of SO188-342KL and core top samples used for the analysis of Ba/Ca and its relation to mixed layer salinity. (For interpretation of the colors in the figure(s), the reader is referred to the web version of this article.)

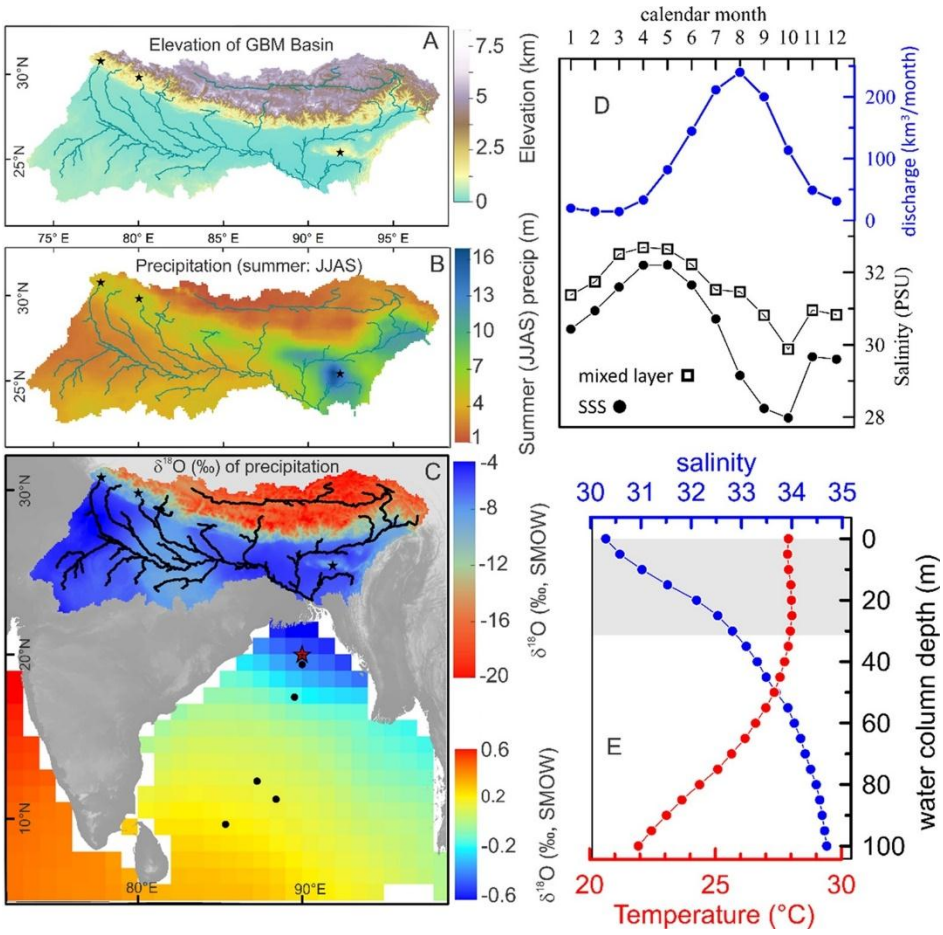

Figure 2. Topography of the GBM Basin and elevation effects on precipitation and $\delta^{18}O$ of precipitation and its manifestation on the surface water of northern Bay of Bengal. A) topographic features of the GBM Basin and the tributaries of the GBM rivers. B) total precipitation between June 1 and September 30 (average from 2014 to 2018). Precipitation data set shown here is a merged satellite-gauge precipitation estimate with a monthly and 0.1 x.0.1 resolution (Huffman, 2017). C)

$\delta^{18}O$ of precipitation (June-to-September) over the GBM Basin (Bowen and Revenaugh, 2003) and monthly averaged $\delta^{18}O$ of Bay of Bengal surface water (0–1 m) in September (Schmidt et al., 1999). The red star and dots indicate the location of SO188-342KL and core top samples used for the analysis of Ba/Ca and its relation to mixed layer salinity. D) Monthly record of GBM runoff (Durand et al., 2011), sea surface salinity (SSS), and mixed layer salinity (Zweng et al., 2018) over the core site. E) Monthly salinity and temperature changes within the upper 100 m of the water column over the core site. The depth of the mixed layer is estimated at 30 m (0–30 m) (gray areas) and is inferred from the temperature profile.

7. 慢速冷却的快速扩张大洋下地壳获得的三维磁条带

翻译人：张伟杰 12031188@mail.sustech.edu.cn

Maher S M, Gee J S, Cheadle M J, et al. ***Three-dimensional magnetic stripes require slow cooling in fast-spread lower ocean crust*** *[J]. Nature, 2021, 597(7877): 511-515.*

https://doi.org/10.1038/s41586-021-03831-6

摘要：洋壳冷却过程中地球磁场被记录下来，形成线性磁异常，并保存了过去 1.6 亿年的极性倒转模式。在辉长岩下地壳中极性区间边界代表等温界限，可以约束冷却过程与地壳增生。快速扩张地壳地震观测、热建模等对地壳内熔体输送和结晶过程的敏感指标---洋中脊附近热量的损失位置和方式产生了相互矛盾的解释。本研究表明岩浆充足的快速扩张地壳的磁性结构需要岩墙-辉长岩过渡带附近的地壳温度保持在大约 500 摄氏度 10 万年。分隔大约 8km 的两个地区接近磁层底凸显了岩脉-辉长岩过渡带 200 米范围内离轴延伸 7-8 公里的近水平极性边界。具有多种极性成分的定向样品可以直接证实相应大约一公里宽的区域内的水平极性边界，并指示其在三个极性间隔内缓慢冷却。我们的结果表明在岩浆充足的快速扩张洋壳中存在一个宽阔的的离轴延伸约 8 公里热轴带，与轴附近几公里内的深部热液冷却模式不相符。

ABSTRACT: Earth’s magnetic field is recorded as oceanic crust cools, generating lineated magnetic anomalies that provide the pattern of polarity reversals for the past 160 million years. In the lower (gabbroic) crust, polarity interval boundaries are proxies for isotherms that constrain cooling and hence crustal accretion. Seismic observations, geospeedometry and thermal modelling of fast-spread crust yield conflicting interpretations of where and how heat is lost near the ridge, a sensitive indicator of processes of melt transport and crystallization within the crust. Here we show that the magnetic structure of magmatically robust fast-spread crust requires that crustal temperatures near the dike–gabbro transition remain at approximately 500 degrees Celsius for 0.1 million years. Near-bottom magnetization solutions over two areas, separated by approximately 8 kilometres, highlight subhorizontal polarity boundaries within 200 metres of the dike–gabbro transition that extend 7–8 kilometres off-axis. Oriented samples with multiple polarity components

provide direct confirmation of a corresponding horizontal polarity boundary across an area approximately one kilometre wide, and indicate slow cooling over three polarity intervals. Our results are incompatible with deep hydrothermal cooling within a few kilometres of the axis and instead suggest a broad, hot axial zone that extends roughly 8 kilometres off-axis in magmatically robust fast-spread ocean crust.

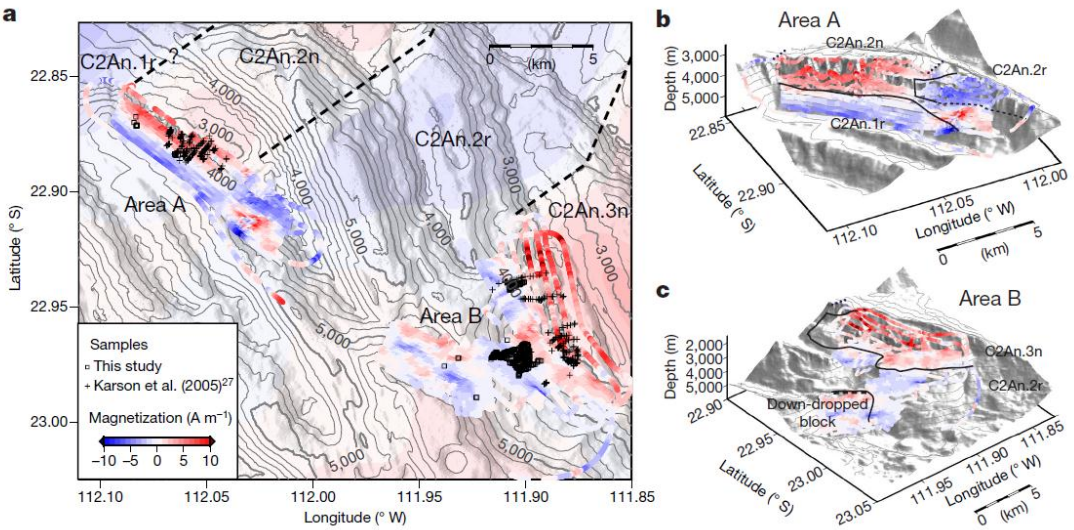

Figure 1. Seafloor magnetization and sample locations at Pito Deep. **a**, Near-bottom magnetization solution of study areas A and B at seafloor elevation (darker shades) overlaid on the background sea surface magnetization solution (lighter shades) from Fig. 1. Dashed lines indicate the locations of polarity boundaries. **b**, Perspective view of area A. Solid lines denote the boundaries of C2An.2n (dashed where speculative). **c**, Perspective view of area B. The solid line indicates the polarity boundary C2An.2r/3n (the apparent complexity of this boundary is a reflection of the bathymetry) and the line with barbs outlines a down-dropped block.

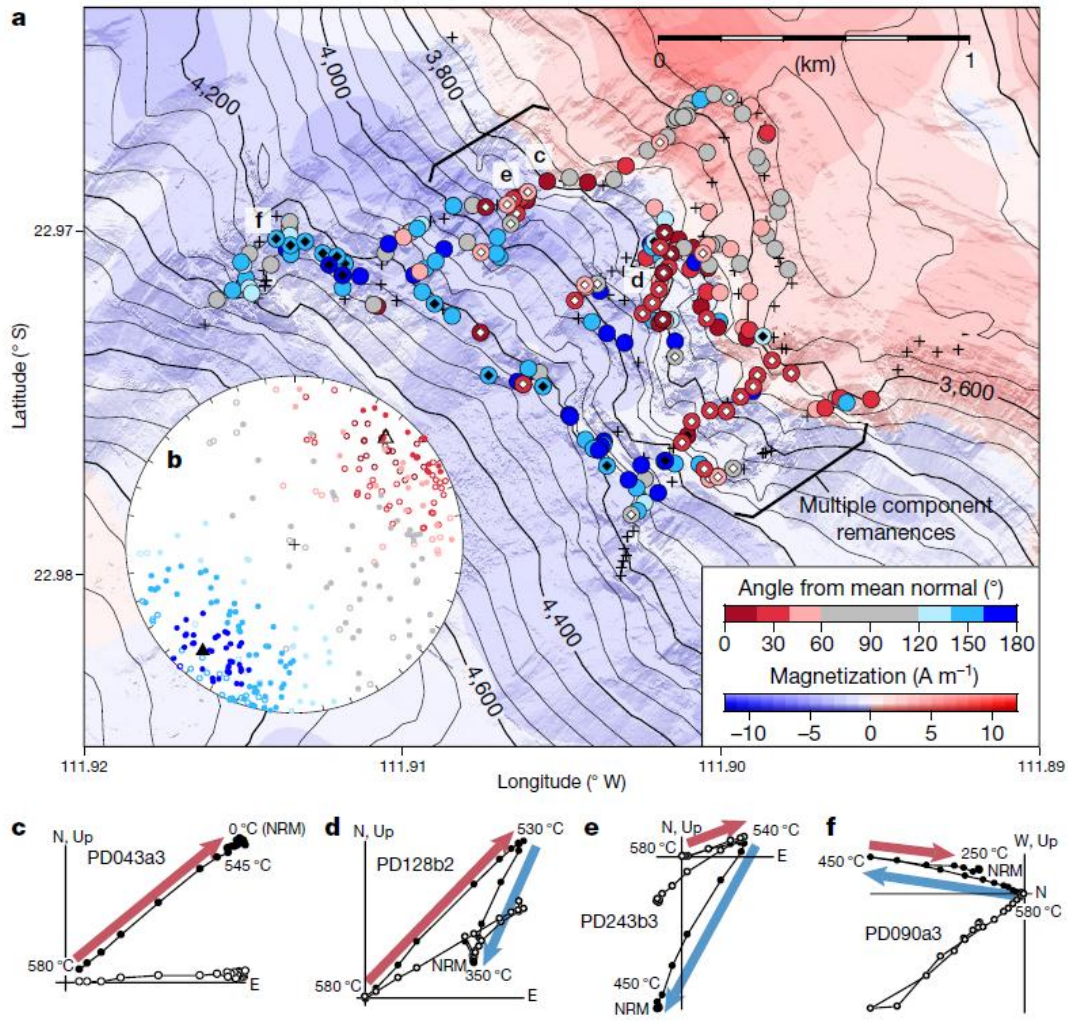

Figure 2. Magnetic polarity of oriented gabbroic samples (n = 229) in area B. **a**, Normal (red) and reverse (blue) polarity samples define a subhorizontal boundary which parallels that of the near-bottom magnetization solution (red-blue background). Low-temperature normal (reverse) overprints are black (white) diamonds. Unoriented samples (n = 84) are shown as plus signs. **b**, Equal-area plot of magnetization components. Open (closed) symbols are upper (lower) hemisphere, colour-coded according to the angle from the mean normal. Averaged directions are triangles. **c–f**, Vector endpoint diagrams illustrating the range of demagnetization behaviour using the samples indicated. Filled (open) circles are projections onto the horizontal (vertical) planes. c, PD043a3 shows a single, normal component (red arrow, up to the right with decreasing temperature). d,e, PD128b2 and PD243b3 show a normal high-temperature component (red arrow), with a low-temperature reverse overprint (blue arrow, down to the left with decreasing temperature) where the overall NRM for d is normal and e is reverse. f, PD090a3 shows a high-temperature reverse component (blue arrow) with a low-temperature normal overprint (red arrow).

8. 北步湾盆地新生代裂陷与反转作用及其与哀牢山-红河剪切带走滑运动的联系

翻译人：刘伟 inewway@163.com

Cheng Y, Wu Z, Zhang J , et al. ***Cenozoic rifting and inversion of Beibuwan Basin and its linkage with the strike-slip movement along the Ailao Shan-Red River Shear Zone*** *[J]. International Geology Review, 2021.*

https://doi.org/10.1080/00206814.2021.2010132

摘要：新生代北部湾盆地位于哀牢山红河剪切带东缘。该盆地的裂陷和反转过程为研究挤压构造驱动大陆裂陷和反转发育的机制提供了重要线索。然而，该盆地的裂陷作用和反转作用尚不明确。本文利用地震资料、断裂时间和位移信息、同裂陷期断裂和等厚图，对北部湾盆地新生代裂陷作用和反转进行了分析。我们的研究结果表明该盆地的构造可划分为三个裂陷期和随后的反转期：(1)古新世初始裂陷阶段，一系列 NE 向的孤立半地堑形成，这表明盆地在该时期以 NW-SE 伸展作用为主导，可能与古南海向南的俯冲拖曳有关有关。(2)始新世裂陷期：除北东向断裂活动明显外，还出现少量东向断裂活动，表明拉张应力场由 NW-SE 向 N-S 方向转移。(3)渐新世裂陷期：E-W 向断裂增强，控制了沉积中心的分布，表明 N-S 向拉张作用主导了该阶段的变形。在始新世至渐新世期间，古近系的伸展应力场由 NW-SE 向 N-S 方向转移，其主要原因可能是哀牢山红河剪切带的左旋走滑运动和古南海的俯冲拖曳有关。(4)渐新世末、中新世末和上新世末的反转期：盆地西部渐新世末期，区域反转较东部强，表明哀牢山红河剪切带所引起的挤压作用向东逐渐减弱。此外，在 Haizhong 凹陷还发生了局部的中新世末期和上新世末期的反转。

ABSTRACT: The Cenozoic Beibuwan Basin is located along the eastern margin of the Ailao Shan Red River Shear Zone (ASRRSZ). The rifting and inversion processes of this basin provide important clues to the mechanism by which extrusion tectonics drive continental rifting and inversion development. However, the rifting and inversion of this basin remain ambiguous. Here, we employ seismic data, information about the time and displacement of faulting, syn-rift fault and

isopach maps to analyse the Cenozoic rifting and inversion of Beibuwan Basin. Our results demonstrate that three stages of rifting and inversion occurred in this basin: (1) During the Palaeocene initial rifting, a series of NE-striking isolated half-grabens formed, which indicated that NW-SE extension dominated in this basin, and the southward slab-pull of Proto-South China Sea (SCS) was the likely cause of the extension. (2) During the Eocene rifting stage, besides significant motion on NE-striking faults, a small number of E-striking faults started to become active, which indicates that the extensional stress field shifted from NW-SE to N-S. (3) During the Oligocene rifting stage, the E-striking faults intensified, and controlled the distribution of the sediment depocentres, which implies that N-S extension dominated the deformation during this stage. The left-lateral strike-slip movement of the ASRRSZ and the slab-pull of the Proto-SCS are suggested to explain the extension stress field shift from NW-SE to N-S during the Eocene to Oligocene. (4) End-Oligocene, end-Miocene and end-Pliocene inversions have been recognized in this basin. The regional end-Oligocene inversion was stronger in the western area than the eastern area of the basin, which suggests that the compression caused by the left-lateral shearing of the ASRRSZ gradually decreased towards the east. In addition, the localized end-Miocene and end-Pliocene inversions occurred in the Haizhong sag.

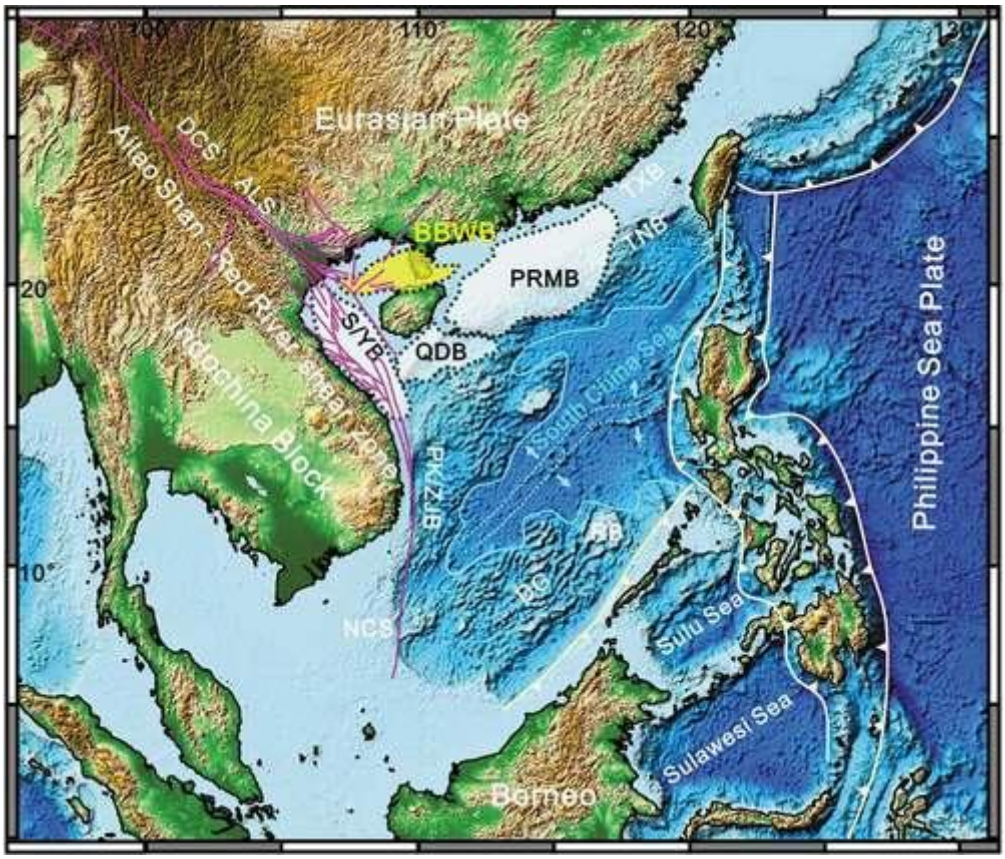

Figure 1 Map showing the regional tectonic framework and the location of the Beibuwan Basin (Modified after Zhang et al. 2013,; Morley, 2016). The location of the ASRRSZ is indicated by the pink lines (the extent of ASRRSZ is modified after Jiang et al. 2017). The extents of the relevant basins are indicated by the grey shaded areas (the shape and location of these basins are modified after Zhang et al. 2013). Abbreviations are TXB, Taixi Basin; TNB, Tainan Basin; PRMB, Pearl River Mouth Basin; BBWB, Beibuwan Basin; QDB, Qiongdongnan Basin; S/YB, Songhong-Yinggehai Basin; PK/ZJB, PhuKhan-Zhongjiannan Basin; NCS, Nam Con Son Basin; DG, Dangerous Grounds; RB, Reed Bank.

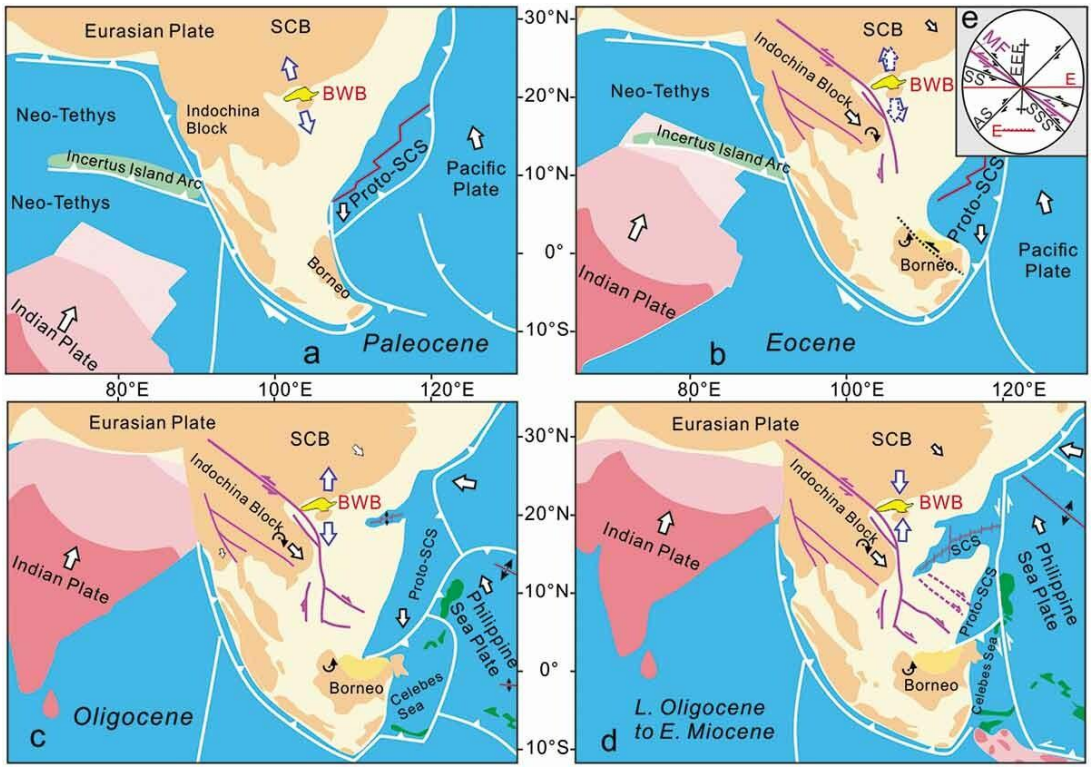

Figure 2. Palaeocene (a), Eocene (b), Oligocene (c) and L. Oligocene to E. Miocene (d) plate tectonic geodynamics models for the Beibuwan Basin (revised from Rangin et al. 1995; Hall 2002; Clift et al. 2008; Hutchison 2010; Li et al. 2012a; Liu et al. 2017). (e) is the angular relation figure between structures that form in an idealized left-lateral simple shear of the ASRRSZ (after Christie-Blick and Biddle 1985; allen and Allen 2013), abbreviations are MF, Master Fault, E, Extension fracture; SS, Synthetic shear; SSS, Secondary synthetic shear; AS, Antithetic shear; EEF, En echelon folds.

9. 东部南极冰盖对晚更新世冰期-间冰期气候驱动的动态响应

翻译人：王浩森 11930841@mail.sustech.edu.cn

Ge S, Chen Z, Liu Q, et al. ***Dynamic response of East Antarctic ice sheet to Late Pleistocene glacial–interglacial climatic forcing*** *[J]. Quaternary Science Reviews, 2022, 277: 107299.*

https://doi.org/10.1016/j.quascirev.2021.107299

摘要：了解东部南极冰盖对晚更新世冰期-间冰期气候循环的响应对于理解全球气候系统和预测未来海平面上升至关重要。本文中，我们在普里兹湾（南极洲东部）近海的三个已定年的岩芯的磁学参数、大块碎屑 Sr–Nd 同位素和 Fe/Ti 比值中发现了过去 530 kyr 显著的冰期-间冰期旋回特性。我们的研究结果表明，与间冰期相比，在南极陆源的冰期发现了大量含钛磁铁矿、较少的放射性钕（ε_{Nd}）以及较高的铁钛比。尤其是在 MIS 11–5 时期，ε_{Nd} 振幅不同于其余记录中的 ε_{Nd} 振幅，这也表现在减弱的矫顽力循环中。根据碎屑 Sr–Nd 分布进行物源识别后，我们识别出两种主要（岩石类型）物源，并推断出两种类型的冰排模式（“侧边”和“通道”），它们遵循兰伯特冰川-阿米利冰架系统（LG-AISS）中的不同路径。第一条沿着连接英格丽德·克里斯滕森海岸的东部路径（侧边），第二条沿着 MIS 11-5 期间通过 LG-AISS 的中央通道（通道）。冰期-间冰期时间尺度上的常规动力学，表现为矫顽力的变化，与模拟的南极冰体积和冰盖运动密切相关，其中，MIS 11–5 期间的第二条通道对应于 340 kyr 较长的片段，即相邻的南极间冰期温度高于目前的温度（MIS 11、9、7 和 5）。因此，我们的记录为东南极普里兹湾地区晚更新世期间冰盖动力学的变化模式提供了迄今为止最清晰的证据，这与中新世晚期-上新世早期约 1.13 Ma（ODP188）期间的冰排变化相吻合。这两个时期相似的冰流变化表明，从稳定的暖期到冷期的突变可以反复触发主要的冰流重构。所提供的数据不仅揭示了冰盖沿经向进退的冰期-间冰期旋回性，而且还揭示了 LG-AISS 细长流域内的纬度变化（横向）。

ABSTRACT: Knowledge regarding the response of the East Antarctic Ice Sheet to glacial–interglacial climatic cycles in the late Pleistocene is critical to understanding the global climate system and projections of future sea level rise. Here, we observed notable glacial–interglacial cyclicity in magnetic properties, bulk detrital Sr–Nd isotopes, and Fe/Ti ratios over the previous 530

kyr in three well-dated gravity cores from the continental rise offshore of Prydz Bay (East Antarctica). Our results show that Antarctic continental sources with more Ti-rich magnetite, less radiogenic epsilon neodymium (ε_{Nd}), and higher Fe/Ti ratios were predominant during glacials in comparison with interglacials. Specifically, the ε_{Nd} amplitude through MIS 11–5 differs from that in the remainder of the records, which is also expressed in the magnetic coercivity cycles with subdued patterns. Following source identification on the basis of the detrital Sr–Nd distribution, we recognize two main (rock type) sources and infer two types of ice drainage flow pattern ("flank" and "channelized"), which follow different pathways in the Lambert Glacier–Amery Ice Shelf system (LG-AISS). The first follows an eastern path connecting the Ingrid Christensen Coast (flank), while the second follows a central channel via the LG-AISS (channelized) during MIS 11–5. Regular dynamics on glacial–interglacial timescales, manifested by changes in magnetic coercivity, are closely related to the modeled Antarctic ice volume and ice sheet movement, in which the second channelized pathway during MIS 11–5 corresponds to a 340-kyr-long episode with contiguous warmer-than-present Antarctic interglacials (MIS 11, 9, 7, and 5). Our records thus provide the clearest evidence so far of variable patterns of ice sheet dynamics during the late Pleistocene in the Prydz Bay sector of East Antarctica, which coincided with similar variation of ice drainage during the late Miocene–early Pliocene at around 1.13 Ma (ODP188). Similar ice drainage changes in these two periods imply that major ice flow reconfiguration can be triggered repeatedly by abrupt changes from a stable warm period to a cold one. The presented data not only reveal glacial–interglacial cyclicity in ice sheet advance and retreat in the meridional direction, but also implicate latitudinal adjustment (lateral) within a thin elongated drainage basin of the LG-AISS.

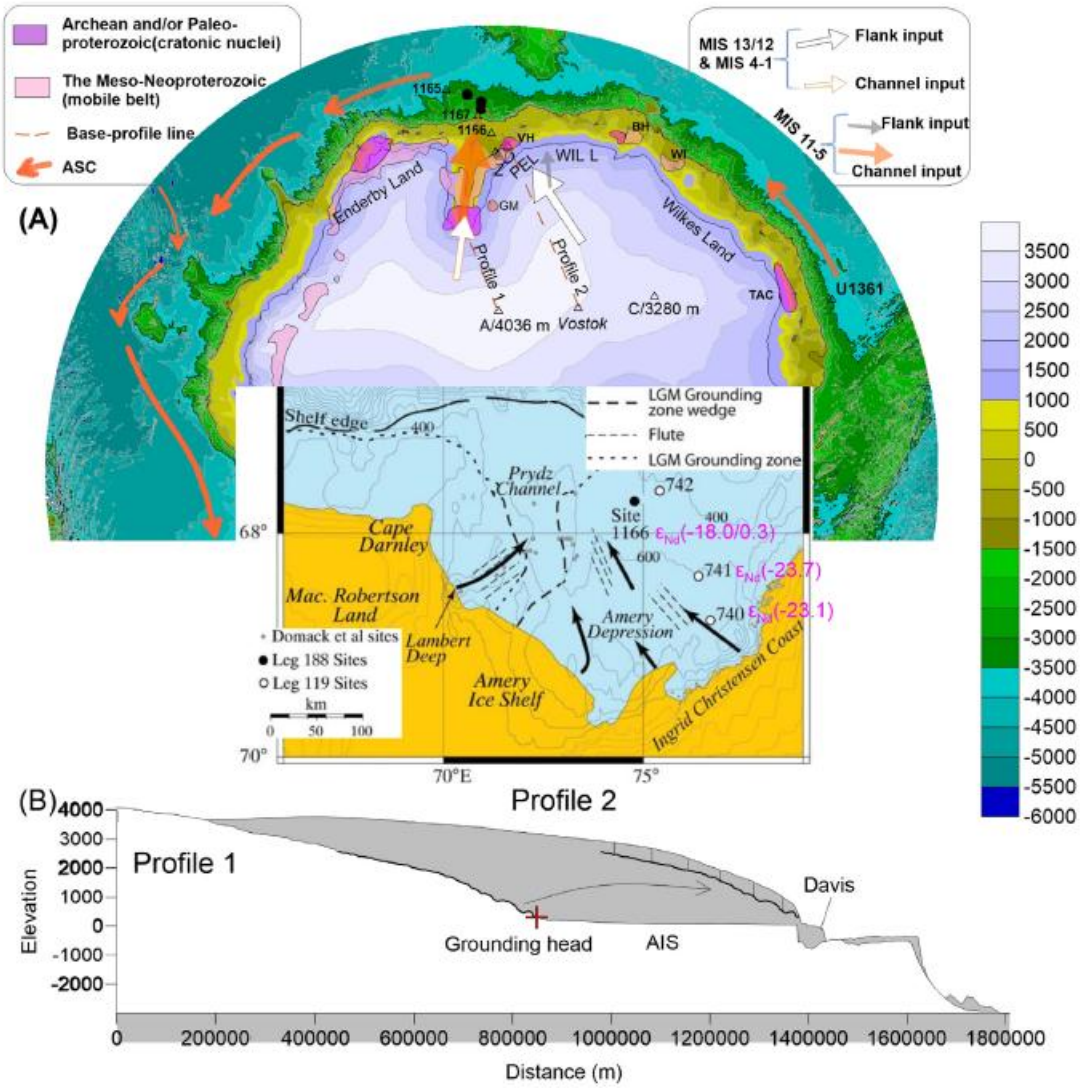

Figure 1. Schematic dynamics of the land-based EAIS during the past 530 kyr. The exposed outcropping ArcheanePaleoproterozoic and Meso-Neoproterozoic rocks around the EAIS are shown. Potential sources of the former include the VH (Vestfold Hills), BH (Bunger Hills) and TAC (Terre Adelie Craton, areal range from Duclaux et al., 2006) via the Antarctic Slope Current. Channelized (MIS 11e5) and flank (MIS 13e12 and MIS 4e1) ice sheet erosion are indicated by colored arrows. Triangles indicate IODP Sites 1165e1167, AT1-3 (ε_{Nd}: 18.5~e21.4) and IODP Site U1361. Other locations are: D: Davis Station, Z: Zhongshan Station, A: Dome A, C: Dome C and Vostok Station. Inset figure to show LGM mega-flute direction and grounding zone delineated by the occurrence of grounding zone wedge. Core top ε_{Nd} from site 740, 741, 1166 are displayed. (B) Baseline profiles 1/2 according to IBCSO version 1. (Bedmap2). Over thickening occurs on the flanks compared with the central channel. The grounding head is located at the turning point of profile 1 in Figure A.

10. 生物磁小体形成的分子机制

翻译人：王敦繁 Dunfan-w@foxmail.com

Komeili, Arash. ***Molecular Mechanisms of Magnetosome Formation [J].*** *Annual Review of Biochemistry, 2007, 76(1):351.*

https://doi. org/ 10.1146/annurev.biochem.74.082803.133444

摘要：趋磁细菌是一类具有利用地磁场传感方向能力的微生物。这一独特的能力是在磁小体的帮助下完成的，磁小体是由脂质双层膜包围的纳米大小的磁性晶体，并通过细胞内专用的细胞骨架组织成链。由于这些磁性晶体的特殊性质，趋磁细菌已在从地球生物学到生物技术的不同学科中得到了广泛的应用。此外，磁小体已成为细菌生物矿化和细胞生物学研究的有力模型系统。本文综述了近年来磁体形成和磁铁矿生物矿化分子机制的研究进展。

ABSTRACT: Magnetotactic bacteria are a diverse group of microorganisms with the ability to use geomagnetic fields for direction sensing. This unique feat is accomplished with the help of magnetosomes, nanometer-sized magnetic crystals surrounded by a lipid bilayer membrane and organized into chains via a dedicated cytoskeleton within the cell. Because of the special properties of these magnetic crystals, magnetotactic bacteria have been exploited for a variety of applications in diverse disciplines from geobiology to biotechnology. In addition, magnetosomes have served as a powerful model system for the study of biomineralization and cell biology in bacteria. This review focuses on recent advances in understanding the molecular mechanisms of magnetosome formation and magnetite biomineralization.

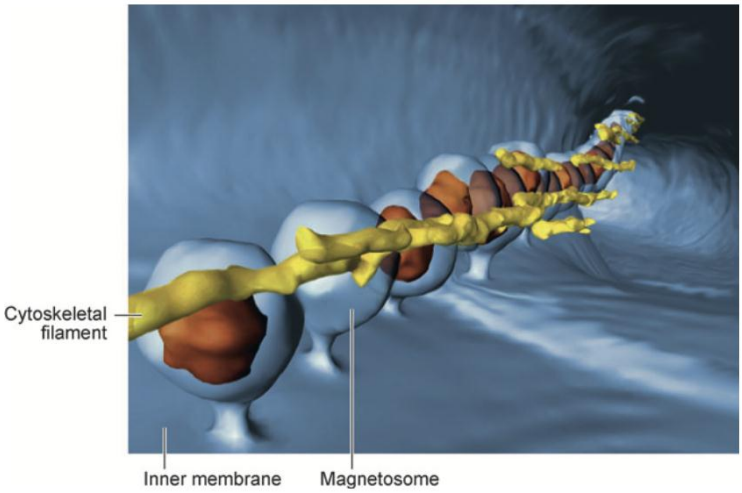

Figure 1. Three-dimensional organization of magnetosomes. An ECT reconstruction of *Magnetospirillum magneticum* sp. AMB-1. The background is the inner membrane, and magnetosomes can be seen as invaginations of the inner membrane. A network of cytoskeletal filaments surrounds the magnetosome chain. Image courtesy of Zhuo Li & Grant Jensen.

11. 全球气候系统中深水形成减少对海洋热收支的瞬态影响

翻译人：张亚南 zhangyn3@mail.sustech.edu.cn

Suzuki T, Komuro Y, Kusahara K, et al., ***Transient Influence of the Reduction of Deepwater Formation on Ocean Heat Uptake and Heat Budgets in the Global Climate System*** [J]. Geophysical Research Letters, 2022, 49(3), e2021GL095179.

https://doi.org/10.1029/2021GL095179

摘要：极地高密度深水的形成和扩散在海洋经向翻转环流中发挥着关键作用，在全球变暖的背景下，深水的形成将会减少。然而，深水形成减少对气候系统可能带来的影响却鲜有研究。文中作者通过一系列的数值模拟，采用人为减少向下水团输送的气候模式来定量评价其对瞬态海洋和气候的响应。研究表明，深水形成的变化不仅对海洋热含量具有不可忽视的影响，对地球大气层顶部的辐射收支也具有重要的作用：高纬海洋深层水形成的减少导致底部海水变暖，海洋表层冷却，随后向外输出的长波辐射也减少。

Abstract: The formation and spreading of dense deepwater in the polar regions play a key role in one of the most important climate systems, namely ocean meridional overturning circulation, and the deepwater formation is projected to decrease under the global warming. However, the impact of the reduced deepwater formation on the climate system has not been explored in detail. Here, we performed a series of numerical experiments with a climate model where the downward water mass transport through the bottom boundary layer is artificially reduced to quantitatively evaluate its impacts on the transient ocean and climate responses. It is demonstrated that changes in deepwater formation have non-negligible impacts on not only ocean heat content but also the Earth's radiation budget at the top of the atmosphere: reduction in deepwater formation in high-latitude oceans causes warming of bottom water, cooling of the ocean surface, and a subsequent decrease in outgoing longwave radiation.

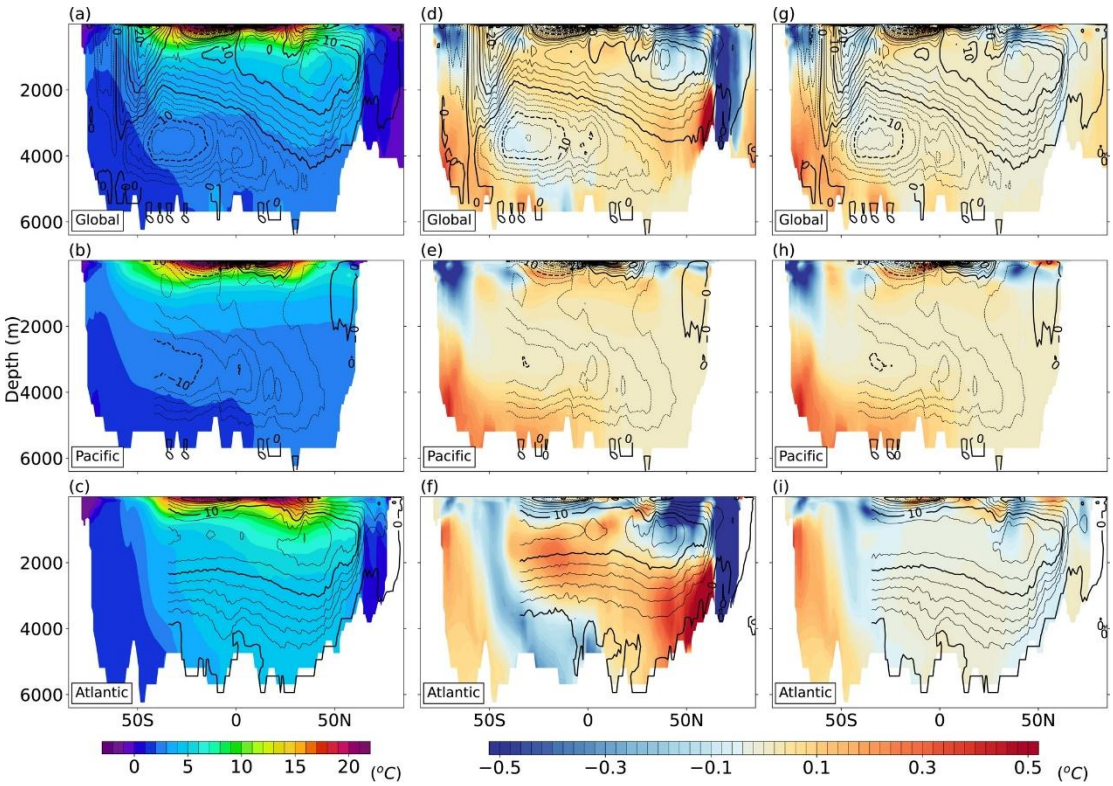

Figure 1. Zonally averaged temperature (colors) for the control experiment (left), and their anomaly (colors) for the b20 m (middle), and the SO_b20 m (right) cases relative to the control in each basin (Global, Pacific, and Atlantic sections) for years 51–70 and the meridional overturning circulation (black contours) for years 1–70. The contour interval is 2 Sv, a dashed contour indicates a negative value, and the interval between thick contours is 10 Sv.

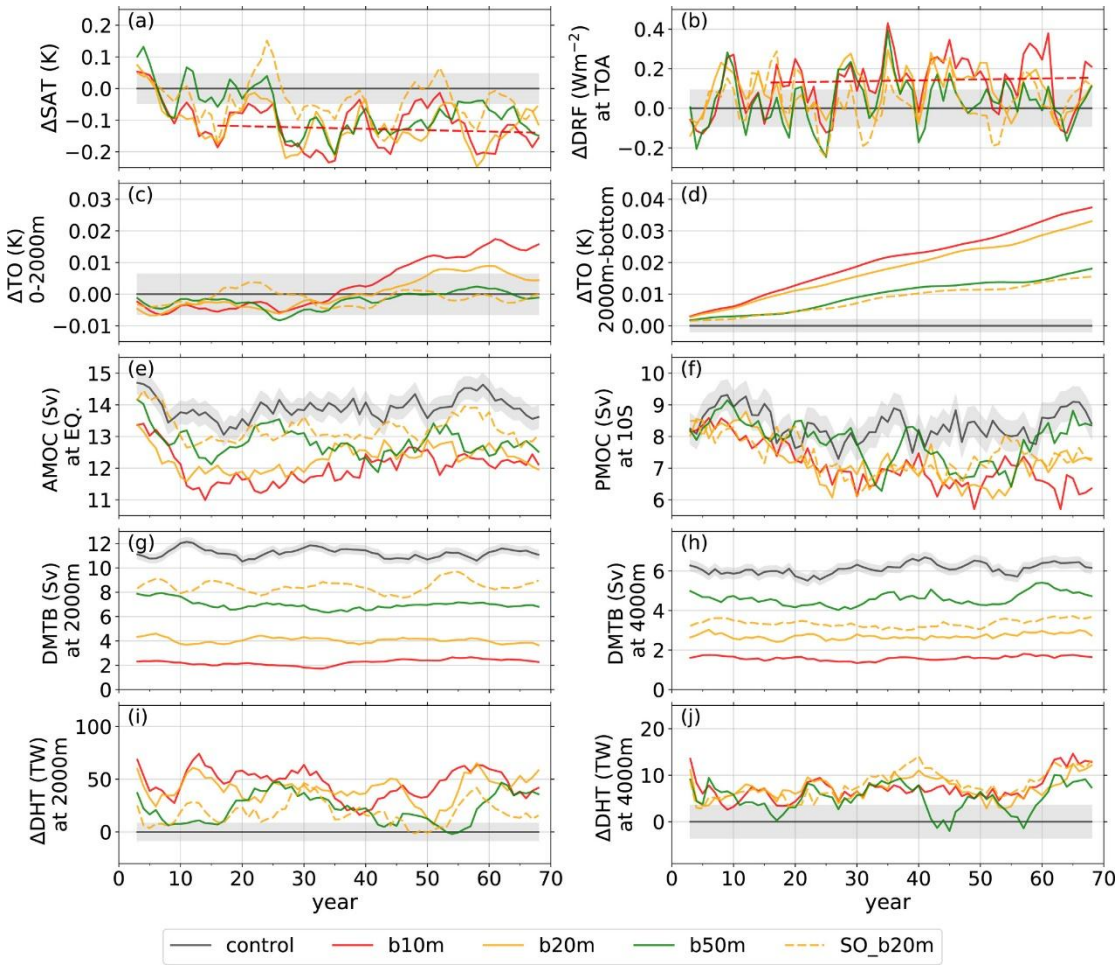

Figure 2. Time series with a 5-year running average of (a) global-mean surface air temperature anomaly, (b) global-mean net downward radiative flux anomaly at the top of the atmosphere, (c) global-mean of the vertically averaged ocean temperature anomaly from the surface to 2,000 m, (d) global-mean of the vertically averaged ocean temperature anomaly from 2000 m to the bottom, (e) southward transport of Atlantic meridional overturning circulation across the equator, (f) northward transport of Pacific meridional overturning circulation across 10 ℃, (g) DMTB across 2,000 m, (h) DMTB across 4,000 m, (i) global downward heat transport (DHT) anomaly at 2,000 m, and (j) global DHT anomaly at 4,000 m. The hatch shows the range of the standard deviations for the Control. The red dashed lines in (a), (b) show the linear approximations over 16–68 years for b10 m.